nature astronomy

Article https://doi.org/10.1038/s41550-025-02628-1

A post-starburst pathway for the formation of massive galaxies and black holes at $z > 6$

Received: 11 September 2024

Accepted: 9 July 2025

A list of authors and their affiliations appears at the end of the paper

Understanding the rapid formation of supermassive black holes in the early Universe requires insights into stellar mass growth in host galaxies. Here we present NIRSpec rest-frame optical spectra and NIRCam imaging from JWST of two galaxies at z > 6, both hosting moderate-luminosity quasars. These galaxies exhibit Balmer absorption lines, like low-redshift post-starburst galaxies. Our analyses of the medium-resolution spectra and multiband photometry show that the bulk of the stellar mass ($\log(M_*/M_\odot) \geq 10.6$) formed in starburst episodes at redshift 9 and 7. One of the galaxies shows a clear Balmer break and lacks spatially resolved Hα emission. It falls well below the star-formation main sequence at $z = 6$, indicating quiescence. The other is transitioning to quiescence; together, these massive galaxies are among the most distant post-starburst systems known. The blueshifted wings of the quasar [O III] emission lines indicate quasar-driven outflow, which possibly influences star formation. Direct stellar velocity dispersion measurements reveal that one galaxy follows the local black hole mass versus σ_* relation whereas the other is overmassive. The existence of massive post-starburst galaxies hosting billion-solar-mass black holes in short-lived quasar phases indicates that supermassive black holes and host galaxies played a principal role in each other's rapid early formation.

Using the near-infrared spectrograph (NIRSpec) onboard the James Webb Space Telescope (JWST)[1], we obtained rest-frame optical spectra at medium resolution of two quasars J2236+0032 and J1512+4422, with redshifts of 6.40 and 6.18, respectively (full coordinates provided in Methods). As clearly shown in Fig. 1a,b (top), Hγ and Hδ are detected in absorption in the NIRSpec data of these systems with accreting supermassive black holes (SMBHs), whereas Hϵ and the red part of Hζ are also present for J2236+0032 due to the bluer rest-frame wavelength coverage of the spectrum. These strong Balmer absorption lines are direct evidence for stellar emission from host galaxies with a predominance of A- and F-type stars, as seen in post-starburst galaxies after short-lived O- and B-type stars have faded away within ~100 Myr. The NIRSpec data also reveal blueshifted broad wing components in the forbidden [O III] λ5008 emission line (Extended Data Fig. 1 and Extended Data Table 1), which are commonly taken as evidence for ionized gas outflow on nuclear scales. The Hα line of J1512+4422 exhibits a double-peaked profile, which can be explained by emission from a rotating accretion disk in the quasar broad-line region (see Extended Data Fig. 2 and Methods for more details).

To model the underlying stellar populations in these two systems, we decomposed the spectra into quasar and host galaxy components. We used multiband imaging data from the JWST near-infrared camera (NIRCam) for this exercise. For J2236+0032, we achieved contiguous coverage from 1 μm to 5 μm (or 1,500 Å to 6,500 Å in the rest frame) with five broadband and three medium-band filters. For J1512+4422, two-band photometry at 1.50 μm and 3.56 μm brackets the Balmer limit. The stellar emission from both host galaxies was successfully detected in all NIRCam images by performing a two-component model fit that includes an unresolved quasar and an extended host galaxy (Extended Data Fig. 3 and Extended Data Table 2). Extended Data Fig. 4 shows that the host galaxies span the 0.2"-wide NIRSpec slit in the dispersion direction. Nonetheless, they are intrinsically compact, with effective radii measured along the semimajor axis no greater than 1 kpc (Extended Data Table 3). In this decomposed multiband photometry,

---

e-mail: masafusa.onoue@aoni.waseda.jp; dingxh@whu.edu.cn

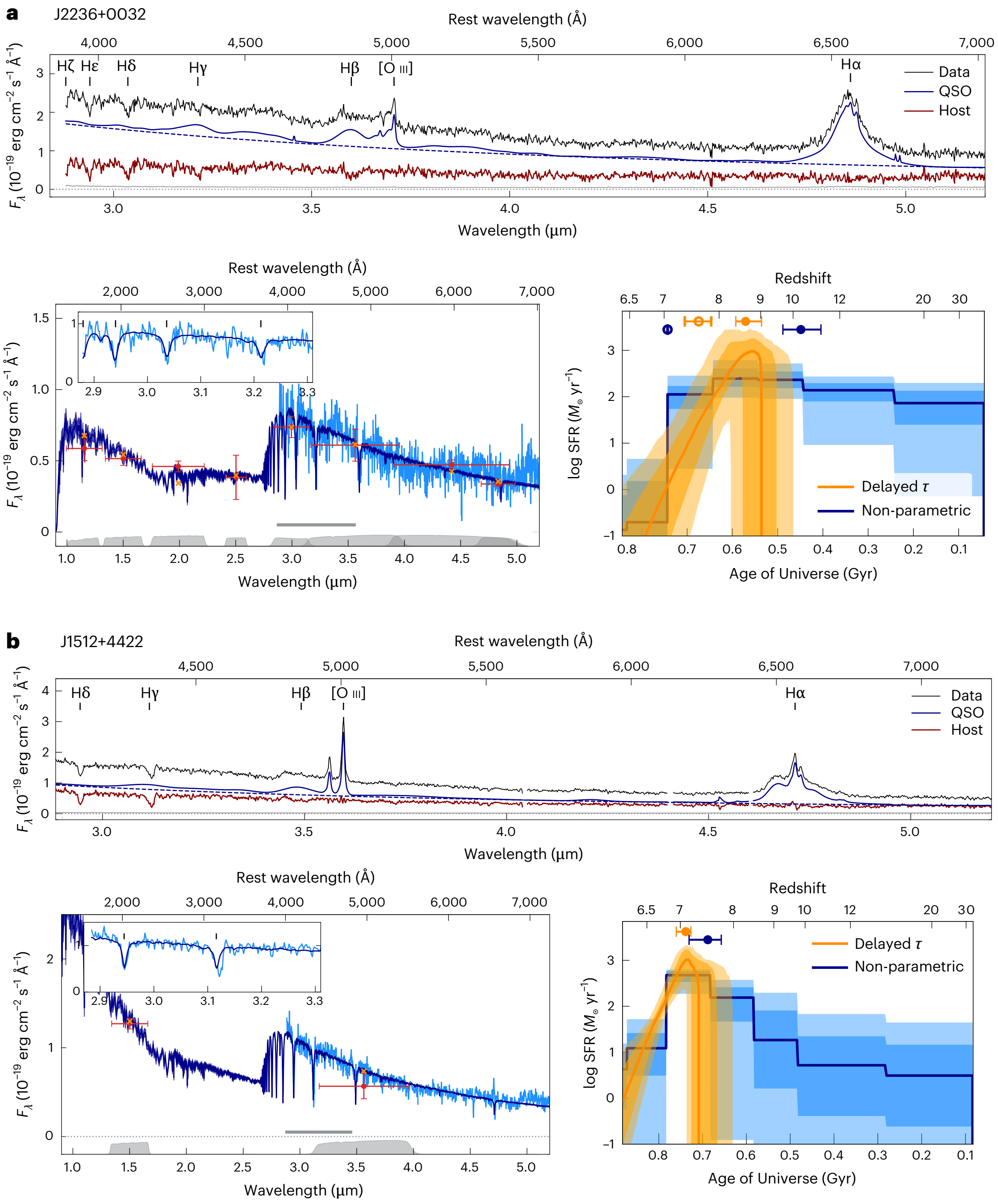

Fig. 1 | JWST NIRSpec G395M spectra of J2236+0032 and J1512+4422. **a**, J2236+0032. **b**, J1512+4422. **a**,**b**, Balmer absorption lines, indicative of a post-starburst phase, are clearly detected. Top: the decomposed quasar and host galaxy components are shown in blue (dashed lines for the power-law continuum and solid lines for the continuum plus emission line model) and red, respectively. The grey solid line represents the error spectrum. Pixels affected by cosmic rays are masked. Flux density F_λ is in units of 10^{-19} erg cm^{-2} s^{-1} Å^{-1}. Bottom left: best-fitting galaxy SED models from Bagpipes according to the delayed-τ SFH model (dark blue). The extracted host galaxy spectrum, scaled to match the decomposed F356W host photometry, is shown in cyan. The grey bar at the bottom shows the wavelength range of the spectrum used in the SED fit. NIRCam photometry is shown with red symbols. Filter transmission curves are displayed at the bottom. Error bars in the x and y directions represent the effective bandwidth and the photometric uncertainties, respectively. Inset: Balmer absorption lines. Bottom right: recovered SFHs (delayed-τ is orange and non-parametric is blue). Solid lines show median posteriors; darker (lighter) shaded regions indicate 16th–84th (2nd–98th) percentile intervals. Filled and open symbols indicate the median posteriors of the formation redshift (z_{form}) and the quenching redshift (z_{quench}), respectively, for each SFH model. Error bars indicate the 16th–84th percentile ranges. QSO, quasi-stellar object.

the clear photometric break at rest frame ~4,000 Å and the lack of an excess in F480M, where Hα falls at $z \approx 6.4$, provide further evidence that J2236+0032 has not been forming stars recently (Fig. 1a, bottom left). Note that these two features are sensitive to different timescales[2], with the break tracing the past 100 Myr of star formation and the Hα emission tracing the past 10 Myr. There is little spatially extended Hα emission in the two-dimensional (2D) spectrum of J2236+0032 (C.L.P. et al., paper in preparation), consistent with the flat F444W − F480M colour of the host. We first model the quasar continuum shape and subtract the continuum plus emission lines to isolate the host galaxy spectra (Fig. 1a,b (top)), as detailed in Methods. We then scale the extracted host spectra to match the decomposed photometry of the host galaxies at 3.56 µm, while accounting for the flux loss from the 0.2"-wide slit.

We then fit the decomposed host galaxy photometry and spectra with stellar population models using Bagpipes, a public spectral fitting code[3,4]. We use the Kroupa initial mass function[5] and two models for star-formation history (SFH): a delayed-τ model where the star-formation rate $\mathrm{SFR}(t) \propto t\exp(-t/\tau)$, with τ denoting the timescale of the exponential decline of star formation, and a non-parametric SFH model with a continuity prior presented in ref. 6. We use 7 time bins for the non-parametric model with bin edges at 0 Myr, 10 Myr, 100 Myr, 200 Myr, 300 Myr, 400 Myr, 600 Myr and 800 Myr before the redshift of observation. The best-fitting spectral energy distribution model (SED) and the recovered SFHs for each target are shown in Fig. 1a,b (bottom). The posteriors of the model parameters are given in Extended Data Table 4 and Extended Data Fig. 5.

In the delayed-τ SFH model, we find that the stellar masses of $\log M_*/M_\odot = 10.80^{+0.03}_{-0.02}$ (±0.08) for J2236+0032 and $\log M_*/M_\odot = 10.64^{+0.04}_{-0.01}$ (±0.02) for J1512+4422 were built up in bursts of star formation, as shown by the rapid rise and fall of their inferred SFHs (Fig. 1a,b, bottom right). Here we report the errors from model-fitting and, in parentheses, those due to the imaging decomposition in the F356W filter (18% for J2236+0032 and 6% for J1512+4422). Other uncertainties due to the assumptions of the initial mass function, the radial profile (Methods) and biases in the assumed SFH shapes are not taken into account. The non-parametric SFH model returns stellar masses consistent with the delayed-τ SFH model for both targets.

The recovered SFHs indicate that the two galaxies experienced starburst episodes at earlier times. The delayed-τ SFH model indicates that J2236+0032 had a peak SFR of $1{,}910^{+870}_{-620}\,M_\odot\,\mathrm{yr}^{-1}$ with a mass-weighted stellar population age of 270^{+20}_{-30} Myr. This age, corresponding to a formation redshift of $z_{\mathrm{form}} = 8.6^{+0.3}_{-0.4}$, represents the time when half of the observed stellar mass had formed. Similarly, the inferred peak SFR of J1512+4422 is $1{,}400^{+520}_{-430}\,M_\odot\,\mathrm{yr}^{-1}$ with a mass-weighted age of 140^{+30}_{-10} Myr ($z_{\mathrm{form}} = 7.1^{+0.2}_{-0.1}$). The non-parametric SFH model yields less extreme yet high SFR peaks with $300^{+140}_{-70}\,M_\odot\,\mathrm{yr}^{-1}$ for J2236+0032 and $480^{+100}_{-120}\,M_\odot\,\mathrm{yr}^{-1}$ for J1512+4422. The inferred ages are 40–130 Myr longer than those from the delayed-τ model. The difference between the two SFH models is attributed to the distinct SFH shape assumed by each SFH model and also to the fact that the present data are not sensitive to stellar populations older than those observable in the rest-frame optical stellar continuum.

In contrast to its previous vigorous starburst activity, the SFR of J2236+0032 dropped sharply, with an e-folding timescale of $\tau = 18^{+9}_{-5}$ Myr. The non-parametric SFH model also indicates a $\gtrsim$2 dex decline of SFR over the past 100 Myr. As a result, both SFH models confirm that the 2σ upper limits of each specific SFR, defined as the ratio of SFR to stellar mass, are $\lesssim 0.1\,\mathrm{Gyr}^{-1}$ and $\lesssim 0.01\,\mathrm{Gyr}^{-1}$ when averaged over the past 100 Myr and 10 Myr, respectively. This galaxy was quenched approximately 100 Myr before the observation, corresponding to a quenching redshift $z_{\mathrm{quench}} = 7.6^{+0.3}_{-0.2}$ (delayed-τ SFH) or $z_{\mathrm{quench}} = 7.1$ (non-parametric SFH), where the quenching time is the epoch when the SFR times the Universe's age drops below 20% of the stellar mass[7]. This rapid quenching is consistent with what has been found for other high-redshift massive quiescent galaxies[8–10].

J1512+4422, which experienced its peak star formation more recently, is currently on the star-formation main sequence, but it is transitioning to quiescence (Fig. 2, left) with an e-folding time like that of J2236+0032. Both SFH models indicate that the specific SFR decreases from $\lesssim 1\,\mathrm{Gyr}^{-1}$ (averaged over the past 100 Myr, 2σ) to $\lesssim 0.2\,\mathrm{Gyr}^{-1}$ (10 Myr). The latter places J1512+4422 around the threshold for quiescence. We conclude that both $z > 6$ quasar host galaxies are among the earliest massive post-starburst galaxies known and were quenching rapidly within the first billion years of the Universe (Fig. 2, right).

We can now chart the mass assembly histories of these two quasar host galaxies and their central SMBHs as a function of cosmic time. As illustrated in Fig. 3 (left), the two galaxies in this study had already grown to stellar masses of $10^{10.5}\,M_\odot$ by redshifts 9 and 7, possibly indicating that they are the evolved descendants of the currently known highest-redshift galaxies hosting an active galactic nucleus (AGN)[11,12]. The rapid stellar mass growth of J2236+0032 and J1512+4422 stands in contrast to the smooth mass growth predicted by theoretical models[13,14].

Another challenge is to explain how the SMBHs that power these quasars formed in the early Universe. These quasars have estimated black hole (BH) masses of $M_{\mathrm{BH}} = 1.1\times10^9\,M_\odot$ and $1.3\times10^9\,M_\odot$, based on broad Balmer emission lines (Methods). If these started as seed BHs growing constantly at the Eddington limit, the seed mass was $\lesssim 10^3\,M_\odot$, depending on the seeding epoch (Fig. 3, middle). This scenario, however, is not strongly preferred, because we estimate sub-Eddington accretion rates at the observed redshifts. An alternative and probably more realistic scenario involves intermittent super-Eddington episodes, as demonstrated in semi-analytical calculations by ref. 15 (Fig. 3, grey lines in the middle panel). This evolutionary scenario, in which the exponential BH accretion mode turns on and off for short periods of time, is generally consistent with studies that indicate that the duty cycle of $z > 6$ quasars—the fraction of time when BH accretion is active—is considerably lower than unity[16,17].

The right panel of Fig. 3 illustrates the evolution of the two galaxies in the M_* versus M_{BH} plane. We assume constant Eddington limit accretion throughout for simplicity. The suppressed stellar mass growth causes the two SMBHs, now observed above the local bulge mass versus SMBH mass relation (grey line), to climb up the co-evolution plane after the starburst phase. This scenario holds unless the SMBHs reached $10^9\,M_\odot$ by the starburst epoch, which is unlikely given the young age of the Universe and the evidence that rapid SMBH assembly typically follows a host starburst in the local Universe[18,19]. These galaxies may also have SFHs like those of known $4 < z < 11$ JWST AGNs[11,12,20], although the pre-starburst SFHs of our sample remain poorly constrained. We also point out that further observations of the local environments are required to address whether these galaxies have completely halted star formation or whether star formation will be rejuvenated once the gas expelled by the quasar feedback falls back or is refilled from their host haloes[21].

The clear detection of stellar absorption lines allows us to measure the stellar velocity dispersion σ_*, a tracer of the depth of the central mass potential. We measure σ_* for the two galaxies as part of the Bagpipes fitting analysis of the SED. The velocity profiles of the stellar population models are convolved with Gaussian kernels to fit the observed Balmer absorption lines. From the delayed-τ SFH model, we recover stellar velocity dispersions of the Balmer lines of $\sigma_* = 290^{+50}_{-60}\,\mathrm{km\,s^{-1}}$ for J2236+0032 and $\sigma_* = 160^{+30}_{-40}\,\mathrm{km\,s^{-1}}$ for J1512+4422. These represent direct measurements of stellar velocity dispersion for quasar hosts at $z > 6$. They are also among the most distant successful measurements of stellar absorption lines for any high-redshift galaxy to date[10,22,23]. We use the penalized pixel-fitting method (pPXF), a widely used tool for measuring σ_*, to validate the Bagpipes results (Methods and Extended Data Fig. 6). For J2236+0032, the inferred σ_* from pPXF agrees with that from Bagpipes. For J1512+4422, however, the inferred σ_* is consistent with an unresolved line within the 1σ uncertainty. We, therefore, adopt a conservative 2σ upper limit of $\sigma_* < 190\,\mathrm{km\,s^{-1}}$, as reported in Extended Data Table 4. Note that the spectrum of J1512+4422 covers only the central region of the host galaxy, which is smaller than the effective radius along the semi-major axis (Extended Data Fig. 4), whereas for J2236+0032, the slit is aligned with the orientation of the host galaxy. This may affect the interpretation of the reported σ_* constraints.

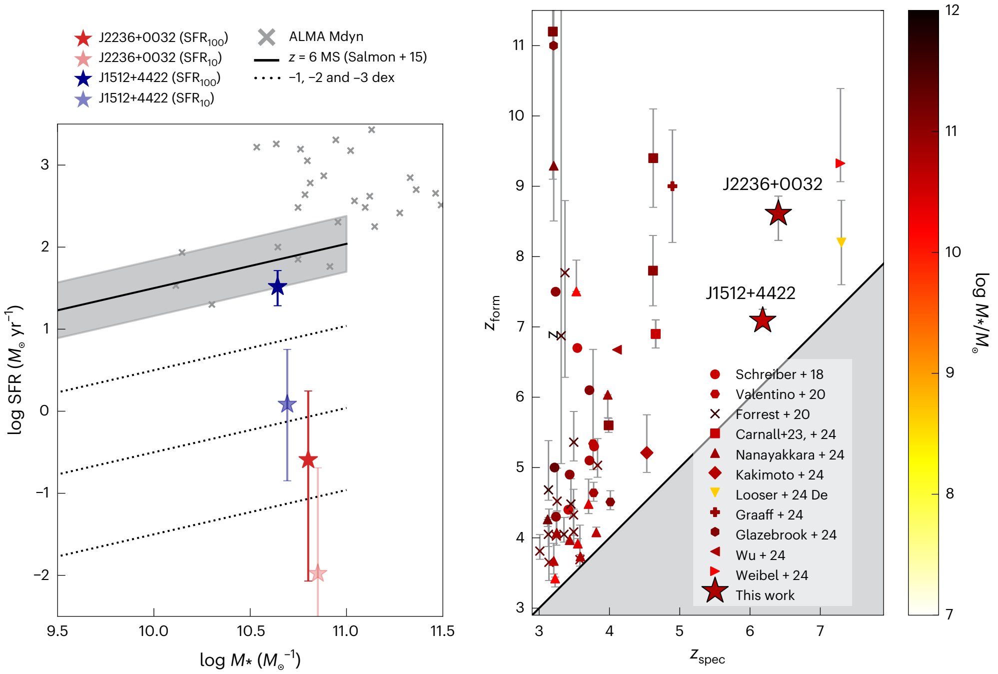

Fig. 2 | Quiescence of the two quasar host galaxies. Left: the stellar mass versus SFR distribution of quasar host galaxies at $z \gtrsim 6$, compared with the star-formation main sequence[72] at $z \approx 6$ and its scatter (black solid line and grey shading). The red and blue symbols represent the median posteriors of the inferred SFR (delayed-τ SFH model) for J2236+0032 and J1512+4422, respectively. For each target, the SFR averaged over the last 100 Myr (SFR_{100}) and 10 Myr (SFR_{10}) is shown as darker and lighter colours, respectively. Error bars indicate the 16th–84th percentile ranges. ALMA dynamical mass measurements and obscured SFR for $z \gtrsim 6$ quasars compiled in ref. 73 are shown as grey crosses. The dotted lines show the star-formation main sequence offset by −1, −2 and −3 dex, respectively. Right: spectroscopic redshift z_{spec} and formation redshift z_{form} of known quiescent galaxies at $z > 3$, colour-coded by stellar mass (more massive galaxies are shown in redder colours). The targets of this work (the delayed-τ SFH model) are the most distant such objects known with stellar mass $\log M_*/M_\odot > 10$. Comparison data are from refs. 8–10,23,45,74–80. Symbols and error bars indicate best-fitting values and their 1σ ranges. We note that several other galaxies with Balmer breaks have been reported at high redshift[81–83].

We show the distribution of the black hole mass and σ_* in Fig. 4, along with local samples and the result for GS-9209, a $z = 4.7$ quiescent galaxy hosting an accreting black hole[8]. J2236+0032 falls on the local relation of ref. 24, whereas J1512+4422 lies slightly above it, indicating that the tight M_{BH}–σ_* correlation observed in the local Universe is being established at $z \approx 6$, with a larger scatter at earlier times. The right panel of Fig. 4 shows that the ionized gas velocity of [O III] does not necessarily trace σ_*, highlighting the need for direct σ_* measurements of high-redshift AGNs to characterize the redshift evolution of the underlying M_{BH}–σ_* relation.

The existence of massive quenched galaxies at high redshifts[8,9,23], as seen by JWST, challenges our understanding of galaxy evolution. Although a tight connection between starburst and AGN activity has been proposed for decades[18,19], it has been unclear whether quasar activity is the primary cause of star-formation quenching. Our discovery of post-starburst galaxies hosting quasars within the first 900 Myr of the Universe adds a layer of intrigue. These observations reveal that, in the high-redshift gas-rich Universe, galaxies can undergo a rapid transition from a starburst phase to a quiescent state while their central SMBHs continue to accrete gas and appear as quasars. Similar cases have recently been reported[8,25–27] at $2 < z < 5$. J2236+0032 and J1512+4422 may represent a brief (a few 100 Myr) phase of quasar-driven galaxy quenching or they could be the cumulative effect of several quasar episodes associated with the earliest-formed SMBHs that quenched star formation. The latter interpretation aligns with the short quasar lifetime indicated in quasar clustering analyses (~1–10 Myr)[17,28] and theoretical models of early SMBH growth[15] (Fig. 3, left). We point out that the high peak SFRs inferred for J2236+0032 and J1512+4422 are comparable to the host SFRs of ultraviolet (UV) luminous quasars in the same redshift range ($\mathrm{SFR} \approx 100$–$1000\ M_\odot\ \mathrm{yr}^{-1}$)[29,30], implying that these two galaxies are in a later quenching phase than the starbursting quasar hosts previously known. Our results shed light on the mechanisms driving quasar activity and its role in galaxy quenching at early cosmic epochs and highlight the need for a better understanding of the mutual growth history of SMBHs and their host galaxies.

Methods

Cosmological model

A standard cosmology with a Hubble constant of $H_0 = 70\ \mathrm{km\ s^{-1}\ Mpc^{-1}}$, a matter density parameter of $\Omega_{\mathrm{m}} = 0.3$ and a dark energy density parameter of $\Omega_\Lambda = 0.7$ is adopted, which gives a scale of 5.51 and 5.62 proper kiloparsecs per arcsecond at $z = 6.4$ and 6.18, respectively. All magnitudes are presented in the AB system. Milky Way dust extinction is negligible at the near-infrared wavelengths of interest and is not corrected for.

Spectroscopic data

The targets presented in this paper, HSC J223644.58+003256.9 (ref. 31) at $z = 6.4$ (hereafter J2236+0032) and HSC J151248.71+442217.5 (ref. 32) at $z = 6.18$ (hereafter J1512+4422) were originally discovered by the Hyper Suprime-Cam Subaru Strategic Program (HSC-SSP)[33]. Their HSC y-band magnitudes and absolute UV magnitudes at rest-frame 1,450 Å are $(y, M_{1450}) = (23.19, -23.75)$ and $(24.16, -22.07)$, respectively. These two quasars were observed in a JWST cycle 1 programme using NIRSpec and NIRCam (GO 1967; PI M. Onoue), which aims to characterize the properties of the central SMBHs and host galaxies of the moderate-luminosity HSC-SSP quasars. The [O III] redshifts of the two targets, based on their narrow components, are consistent with the rest-frame UV measurements ($|z_{\mathrm{UV}} - z_{[\mathrm{O\,III}]}| \le 0.01$; Extended Data Table 1), as detailed below.

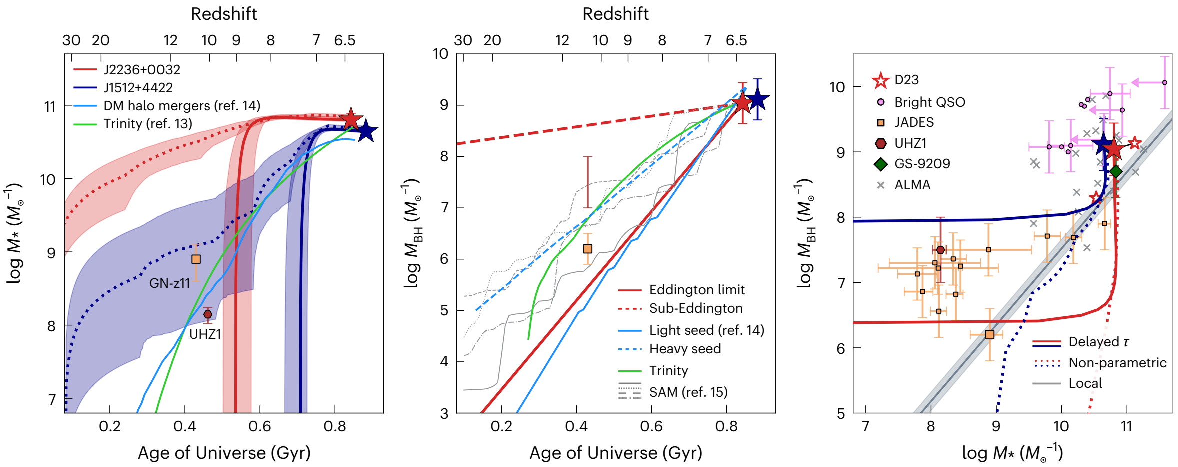

Fig. 3 | Growth pathways of the two quasar host galaxies and their SMBHs. Left: stellar mass assembly as a function of cosmic time based on the delayed-τ SFH models (solid lines) and non-parametric SFH models (dotted lines). The 16th–84th percentile range is indicated by the shaded region for each model. For comparison, the average growth curve from the Trinity simulation[13] is shown in green, and that based on the dark matter halo merger history from ref. 14 is shown in cyan. Both model curves, fine-tuned to reproduce the observed stellar mass of J2236+0032, are smooth and in contrast to its inferred mass growth, which reaches $>10^{10.5}\,M_\odot$ by $z \approx 8$. Two of the known $z > 10$ galaxies hosting AGN are also presented (GN-z11 (ref. 11) in orange and UHZ1 (ref. 12) in brown). Middle: BH mass assembly as a function of time. The red lines show cases in which J2236+0032 continuously accretes at the Eddington limit (solid) or at the observed Eddington ratio (10%; dashed), both with 10% radiative efficiency. The blue lines show the models of ref. 14, where the seed BH for J2236+0032 is a light seed of 50 $M_\odot$ (solid line) or a heavy seed of $10^5\,M_\odot$ (dashed line). The four grey lines show the semi-analytical model from ref. 15, where seed BHs grow by changing Eddington ratios (including super-Eddington accretion rates) for short periods of time. The four BHs presented here are a representative sample of BHs that reach ~$10^9\,M_\odot$ by $z = 6$. These model growth curves are scaled to match the BH mass of J2236+0032. Right: evolution in the M_{BH} versus M_* plane (solid lines: delayed-τ SFH; dotted lines: non-parametric SFH model). Luminous quasars whose host stellar emission is detected with JWST[84–86] (pink) and faint AGNs from the JWST Advanced Deep Extragalactic Survey[20] (orange, with smaller symbol sizes than GN-z11) are shown for comparison. Quasar systems with ALMA dynamical masses and Mg II-based M_{BH} compiled by ref. 73 are shown as grey crosses. The $z = 4.7$ quiescent galaxy GS-9209 (ref. 8) is shown in green. The stellar and BH masses of the two $z > 6$ quasar host galaxies in the earlier study of ref. 34 (D23), which includes J2236+0032, are shown as open red stars. The local bulge mass versus BH mass relation from ref. 24 is shown as the grey line. Error bars represent 1σ ranges in all panels. DM, dark matter; JADES, JWST Advanced Deep Extragalactic Survey; SAM, semi-analytical model.

The JWST NIRSpec observations were executed on 28 October 2022 for J2236+0032 and 14 February 2023 for J1512+4422. The targets were aligned onto the 0.2"-wide S200A2 slit using the wide-aperture target acquisition method. Data were taken with the medium-resolution G395M grating, which covers 2.87–5.27 µm. For our emission and absorption line measurements, we used the spectral resolution $R = 750$, which is provided in the JWST documentation. Note that both host galaxies were extended along the dispersion direction of the S200A2 slit, which is 0.2" wide, as shown in Extended Data Fig. 4. The exposure for J2236+0032 was divided into 45 groups at each of three primary dither positions without subpixel dithers, amounting to 1,970 s. The NRSIRS2RAPID mode was used for detector read-out. The y-band magnitude of J1512+4422 is 1 mag fainter than J2236+0032, so we integrated longer, using the NRSIRS2 detector read-out mode. The target was observed with 18 groups each at three primary dither positions, which was repeated twice to achieve a total exposure time of 7,878 s.

Here we briefly describe the NIRSpec data reduction in this paper; the details are given in ref. 34. The raw (uncal) spectroscopic data were downloaded from the Mikulski Archive for Space Telescopes and processed with JWST pipeline v.1.17.1 with parameter reference files JWST_1100.PMAP (J2236+0032) and JWST_1069.PMAP (J1512+4422), as registered in the JWST Calibration Reference Data System (https://jwst-crds.stsci.edu). The 1/*f* noise in the 2D spectra was subtracted after the stage 1 pipeline reduction using a public code implemented in msaexp (ref. 35). For each target, the point-source pathloss correction was applied during the stage 2 pipeline reduction to make sure that the quasar light from the targets was fully flux-calibrated. The processed 2D cal spectra at each dither position were stacked using the stage 3 pipeline with inverse-variance weighting. One-dimensional spectra were extracted with a 6-pixel-wide (0.6" wide) box-car aperture.

Photometric data

JWST broadband NIRCam imaging data were also available for the two targets. Images taken with two broadband filters (F150W and F356W) were obtained for each target in GO 1967. These two filters were chosen to straddle the redshifted Balmer break. J2236+0032 was also observed in another six photometric filters (F115W, F200W, F250M, F300M, F444W and F480M) in cycle 2 (GO 3859; PI M. Onoue). These eight-band photometric data cover the rest-frame wavelength range from 1,550 to 6,530 Å. The Hα line of J2236+0032 falls in the medium-resolution F480M filter, which makes it possible to address the Hα emission strength of the host galaxy. The raw imaging data were processed with the same procedure as in ref. 34 with the pipeline v.1.8.5. For both the short-wavelength (F115W, F150W and F200W) and long-wavelength (F250M, F300M, F356W, F444W and F480M) data, single-visit images from the stage 2 pipeline were stacked with a pixel scale a factor of 2 smaller than that of the detector during the RESAMPLE step of the stage 3 pipeline processing. The final pixel scales were 0.0153" for short-wavelength and 0.0315" for long-wavelength images. The astrometry was calibrated against GAIA Data Release 3 stars within the field of view of the target images.

Two-dimensional image decomposition of NIRCam data

We used galight[36], which uses the image modelling capabilities of Lenstronomy[37] to separate the bright quasar light from the stellar light of the underlying host galaxy. A scaled point spread function (PSF) was used to represent the unresolved quasar emission. The radial profile of the stellar emission from the host galaxy was modelled by a 2D Sérsic profile convolved with the PSF model. This software has been tested with many astronomical images from the Hubble Space Telescope[36] and the ground-based Subaru/HSC[38]. D23 shows that the stable and sharp JWST PSF makes it possible for galight to detect quasar host galaxies[34,39]

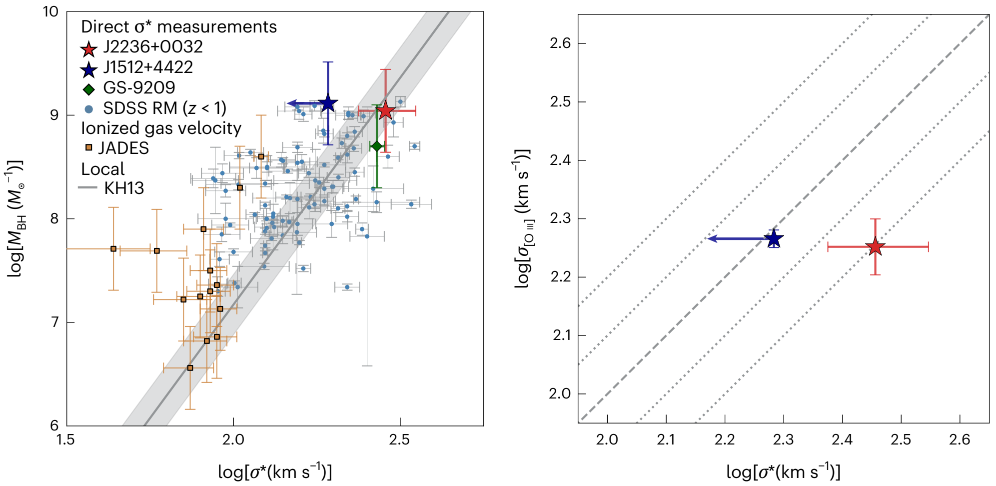

Fig. 4 | Stellar velocity dispersion (σ_*) measurements. Left: distribution of M_{BH} versus σ_*. Red and blue symbols represent J2236+0032 and J1512+4422, respectively. The green symbol shows GS-9209 (ref. 3), and orange symbols show the JADES sample[20]. Cyan symbols show the $z < 1$ quasars from the Sloan Digital Sky Survey reverberation mapping project[87]. Error bars represent 1σ ranges, except for σ_* of J1512+4422, which is shown as a 2σ upper limit (see text for details). Note that σ_* measurements are based on stellar absorption lines for our targets and GS-9209, whereas the JADES sample use the ionized gas velocity dispersion measured from the [O III] emission lines ($\sigma_{[\mathrm{O\,III}]}$). The grey line and shading show the local relation and its scatter[24] (KH13). Right: comparison of σ_* estimated from the Balmer absorption lines with $\sigma_{[\mathrm{O\,III}]}$. The diagonal dashed line is the one-to-one relation, and the dotted lines indicate the cases where the [O III] velocity dispersion is offset from the spectroscopic σ_* from −0.2 to +0.2 dex in steps of 0.1 dex. For J2236+0032, σ_* is larger than $\sigma_{[\mathrm{O\,III}]}$ by approximately +0.2 dex. SDSS RM, Sloan Digital Sky Survey reverberation mapping project.

at $z = 2$–6. The shape of the PSF, which was crucial in the decomposition analysis, was based on bright isolated stars detected in the same image as the quasars. We applied each of these PSF models in turn when fitting the target images and selected the top five PSF models based on χ^2. The imaging decomposition results reported in this work are based on the best-fitting model with their uncertainties derived from the dispersion in the host properties from these five PSF models. During the fitting process, we used a fixed Sérsic index of $n = 3$ for the two target galaxies. The choice of this Sérsic index was motivated by a morphological study of high-redshift quiescent galaxies from ref. 40. We also performed the imaging decomposition analysis with the Sérsic index fixed to $n = 1$, 2 or 4; however, we found no substantial difference in the goodness of fit between the four cases because of the degeneracy between the unresolved quasar emission and the host emission, especially given how compact the host galaxies of our two targets are. The imaging decomposition analysis was performed separately for the images in each of the eight (J2236+0032) and two bands (J1512+4422).

The results of the 2D image decomposition are reported in Extended Data Table 2. We successfully recovered the host stellar emission from both targets across all filters. The original NIRCam images and the host images after PSF subtraction are shown in Extended Data Fig. 3. J2236+0032 and J1512+4422 show the brightest stellar emission in F356W among the 12 targets observed in our cycle 1 programme. Extended Data Table 3 shows that both host galaxies have compact morphologies in the F356W images, with effective radii (R_{eff}) of 0.10–0.17 arcsec, corresponding to $R_{\mathrm{eff}} = 0.55$–0.96 proper kpc. The R_{eff} values measured in other filters were also below 1 kpc, supporting the robustness of the fitting results. In addition to their compactness, these galaxies exhibit moderately elongated shapes, with minor-to-major axis ratios $q = 0.3$–0.5. The full results for our cycle 1 and cycle 2 data will be presented in ref. 41.

Spectroscopic decomposition for the NIRSpec data

We decomposed the NIRSpec rest-frame optical spectra into quasar and host components. We first performed continuum plus emission line spectral fitting for the spectra obtained to model strong emission lines, a power-law quasar continuum and the iron pseudo-continuum, which should be subtracted for the host galaxy analysis. Note that stellar emission was not taken into account in this step. For this purpose, we ran a public spectral fitting tool QSOFitMORE (v.1.2.0)[42] with custom modification to fit the continuum and emission lines simultaneously. We manually masked pixels that were affected by the high-order Balmer absorption lines, allowing us to fit broad emission components for Hγ (J2236+0032 and J1512+4422) and Hδ (J1512+4422). Each of these two Balmer emission line components was fitted with a single Gaussian profile. As is also described by D23, J2236+0032 needs one Gaussian profile for Hβ and one narrow and one broad component for each of the [O III] doublet lines.

To subtract the quasar continuum emission from the line-free spectra, we adopted a single power-law function, $f_\lambda \propto \lambda^{\alpha_\lambda}$, where α_λ represents the continuum slope. For J2236+0032, we fitted a single power-law function to the decomposed quasar NIRCam photometry in the three filters that encompass the NIRSpec data (F300M, F356W and F444W). The host galaxy spectrum was extracted by subtracting the emission line (including iron) plus power-law quasar model from the original spectrum. To account for extended emission falling outside the S200A2 slit, we rescaled the decomposed host spectrum upwards by 7% to match the host galaxy photometry in F356W. After performing the initial host SED fitting analysis, we iterated the emission line fitting and host extraction using the best-fitting host SED model, as detailed later in this section. In the second iteration, we modelled the line and continuum emission using the spectrum from which the galaxy model had been subtracted. We found that this iterative procedure improved the modelling of the broad Balmer lines, which were affected by stellar absorption. The resulting quasar continuum slope is $\alpha_\lambda = -1.89 \pm 0.26$. The host SED properties reported in this paper are based on the spectrum with the quasar continuum subtracted using this updated model.

For J1512+4422, we initially fixed α_λ to −1.7, a typical value for low-redshift quasars[43]. We then updated it to $\alpha_\lambda = -2.23 \pm 0.01$ based on the second iteration of the QSOFitMORE fitting, using the spectrum with the initial host galaxy model subtracted. The scale factor of the continuum model needed some consideration. We first scaled the single power-law so that the emission line plus power-law quasar model matched the F356W quasar photometry (22.51 ± 0.05 mag). However, when we did so, the equivalent widths (EWs) of the Balmer absorption lines became too large to be reproduced with the stellar population models. One could avoid this issue by assuming a flatter α_λ;

however, when we did so, the extracted host continuum became too blue to be reproduced by galaxy SED models. This is also the case when the assumed Sérsic index was changed to $n = 1$, 2 or 4. We, therefore, allocated further flux to the quasar component to derive meaningful host SED characteristics. After some experimentation, we found that adding +0.2 mag to the F356W quasar photometry resulted in a satisfactory result. This inconsistency between the imaging and spectroscopic decomposition is potentially due to a non-negligible contribution from unresolved galaxy emission to the quasar photometry. Given the potential oversubtraction of the quasar emission, the stellar population analysis of J1512+4422 warrants caution. Multiband or higher-resolution imaging follow-up observations are required.

Strength of Balmer absorption and Balmer break

Here we report model-independent measures of the strength of Balmer absorption lines and the Balmer breaks. To characterize the strength of the Balmer line absorption, we measured the Hδ rest-frame EW for both the original spectrum and the decomposed host galaxy-only spectrum. Following the procedure of ref. 44, we measured the inverse-variance weighted mean continuum flux at two wavelength windows, [4,030, 4,082] Å, and [4,122, 4,170] Å, and interpolated them to estimate the local continuum at the wavelength of Hδ. Using the decomposed host galaxy spectrum, we derived EW(Hδ) = 9.5 ± 0.3 Å for J2236+0032 and 9.1 ± 0.1 Å for J1512+4422, which meet the definition of quiescent galaxies adopted in ref. 45 (>4 Å). The Hδ EW of the original spectrum before subtracting the quasar continuum was 2.8 ± 0.1 Å and 3.9 ± 0.1 Å, respectively.

We also measured the strength of the Balmer break for J2236+0032 using the decomposed photometry. The F250M and F300M medium-band filters cover the rest-frame wavelengths of 3,259–3,506 Å and 3,825–4,266 Å, thus straddling the Balmer break. The ratio of the flux density at these two filters can serve as a proxy for the Balmer/4,000 Å break indices in the literature. We took the ratio of F_λ values and derived F_λ(F300M)/F_λ(F250M) = 1.9 ± 0.8. The corresponding ratio for F_ν (in units per unit frequency) is 2.8 ± 1.2. According to ref. 46, this value is comparable to those expected for a single stellar population with an age of several 100 Myr (see their Extended Data Fig. 1), which is broadly consistent with the age estimate from our SED fitting analysis (Extended Data Table 4). Note that the original wavelength windows applied in ref. 46 are [3,145, 3,563] Å and [3,751, 4,198] Å. Also note that there may be a contribution from [Ne III] λ3867 to the F300M photometry. We did not measure the same index for J1512+4422, as the photometric data were limited to F115W and F356W.

Recently, ref. 47 suggested that an AGN can mimic the stellar Balmer break and Balmer absorption when the nuclear radiation is absorbed by dense gas clouds. This scenario may explain the continuum shape and the apparently large stellar masses and high abundance of the dust-obscured compact 'little red dot' galaxies in the early Universe. We argue that such a model is not a good fit to the two quasars in this paper, which show similar features. The photometric SEDs in Fig. 1 are based on the spatially extended components of the two sources. Therefore, the clear Balmer break in J2236+0032 does not originate from AGN emission, which is expected to be unresolved. The constraint on the Balmer break for J1512+4422 is rather weak, and this object shows a double-peak profile in Hα emission (see 'Double-peak profile in Hα emission from J1512+4422'); however, the broad Balmer absorption of the high-redshift little red dot galaxies is mostly blueshifted with respect to the narrow emission lines[47], whereas Hα for J1512+4422 has a higher peak at the bluer side than its redder side. Given these differences, the arguments of ref. 47 do not be apply to J2236+0032 and J1512+4422, at least not to the same extent as to little red dots.

Modelling the stellar populations of quasar host galaxies with Bagpipes

We performed spectrophotometric fitting for the two quasar host galaxies using Bagpipes, a public spectral fitting code used to model galaxy SEDs[3,4]. We limited the spectral fitting window to rest frame ≤4,800 Å, because there are no apparent absorption lines from the host galaxy at longer wavelengths. We also found that the use of the full NIRSpec data overly biases the SED fitting towards the rest-frame optical wavelengths, as the relative weight of the NIRCam photometry, particularly F150W, which is sensitive to the rest-frame UV wavelengths, becomes reduced. Moreover, the absorption line fitting was not optimal. The resulting NIRSpec wavelength ranges for J2236+0032 and J1512+4422 are $\lambda_{\rm rest}$ = 3,890–4,800 Å and 4,010–4,800 Å, respectively. We masked the red wing of the Hγ absorption line of J1512+4422 over $\lambda_{\rm rest}$ = 4,344–4,369 Å because this range cannot be well reproduced by our analyses. A potential reason for this poor fit is that J1512+4422 exhibits a distinct line profile (Extended Data Fig. 2) that is not represented by Gaussian profiles. We used the default stellar population synthesis models of Bagpipes, which are based on the 2016 version of the BC03 models[48,49] with the Kroupa initial mass function[5]. The same function is commonly adopted in analyses of massive quiescent galaxies in the literature. The lower and upper cutoff masses are 0.1 $M_\odot$ and 100 $M_\odot$, respectively. These models use the MILES stellar spectral library[50], which has a wavelength resolution of ~2.5 Å in 3,525–7,500 Å.

We explored the SFH of the target galaxies assuming two models: delayed-τ SFH (SFR(t) ∝ $te^{-t/\tau}$), where τ represents the decay timescale, and the non-parametric continuity SFH model of ref. 6. The choice of the delayed-τ SFH is appropriate for the target galaxies because we aimed to characterize the SFHs of galaxies that are expected to decline after a major star-forming epoch. The non-parametric SFH model is more flexible than the parametric SFH, while the continuity prior implemented works against a rapidly quenched SFH. During the SED fitting process, the stellar age was limited to the ranges 10–840 Myr (J2236+0032) and 10–800 Myr (J1512+4422) using a logarithmic prior. These upper limits correspond to the age of the Universe at the quasar redshifts. The stellar mass was allowed to vary within the range $\log(M_*/M_\odot)$= 5–15 using a logarithmic prior. Dust attenuation was modelled with the Calzetti law[51]. A logarithmic prior was used for the rest-frame V-band attenuation over the range A_V = 0.01–5 mag. The stellar metallicity was fixed to 0.5 $Z_\odot$, a value expected from extrapolation of the stellar mass versus gas-phase metallicity relation of z = 4–10 galaxies[52]. The redshift has a Gaussian prior, given by the measured [O III] redshift and its estimated uncertainty. A noise scaling factor (×1–10) was implemented to match the flux uncertainty output by the JWST pipeline to the actual variation of the data relative to the model. Note that the recovered scaling factor for the two galaxies in this study (1.4–1.9) is broadly consistent with what ref. 8 found for their quiescent galaxy, indicating that the error spectrum produced by the JWST pipeline underestimates the actual signal fluctuation. The stellar velocity dispersion σ_* was measured by convolving the stellar continuum models with Gaussian kernels in velocity space. We allowed σ_* to vary within the range σ_* = 1–1,000 km s^{-1}. The instrument resolution ($\sigma \approx 170$ km s^{-1}) at the wavelengths of the Balmer absorption lines was taken into account by referring to the JWST User Document. Logarithmic priors were used for these two parameters. Finally, nebular emission lines were taken into account for J2236+0032 with the ionization parameter fixed to log U = −3. This nebular component was designed to provide an upper limit of the Hα flux.

We reran our SED fitting for J2236+0032 by fixing the stellar metallicity from 0.1 to 1 $Z_\odot$ with the delayed-τ SFH model, finding that the choice of the stellar metallicity did not largely affect the stellar mass estimate. The mass-weighted age changed from 240 to 350 Myr (50th percentile), and the recovered SFH satisfied the quiescent threshold for all cases, thus, doing this did not affect the main results of this paper. Note that the goodness of fit did not largely change from the fiducial 0.5 $Z_\odot$ model ($|\Delta\chi^2_{\rm reduced}| < 0.2$), indicating that a direct estimate of stellar metallicity is challenging with the existing data.

We note that the σ_* measurements of the two galaxies based on Balmer absorption lines should be interpreted with caution. J2236+0032 aligns well with the major axis of the host, whereas for J1512+4422, the slit is tilted by approximately 60 degrees relative to the disk-like elongated component of the stellar emission. In addition, the kinematics of A- and F-type stars, which dominate the observed spectra of the two galaxies at rest-frame optical wavelengths, may not accurately represent the kinematics of the older stellar populations that typically dominate the total mass of the galaxy. To achieve more precise σ_* measurements, integral field spectroscopy with JWST or the Atacama Large Millimeter Array (ALMA) as well as observations of non-hydrogen σ_* tracers[53] (such as the calcium triplet $\lambda\lambda$8498, 8542, 8662) are necessary. We address the systematic difference between Bagpipes and pPXF measurements in section 'Comparison of different fitting methods'.

Comparison of different fitting methods

In addition to Bagpipes, we also fitted the JWST data for the two galaxies with pPXF[54], which is widely used in the characterization of kinematics and stellar population of galaxies. Here we adopt the FSPS stellar library[55,56] to model the same photometric and spectroscopic data as in the Bagpipes analysis. To estimate the uncertainties, we performed Monte Carlo resampling of the spectrum using the error vector, incorporating the noise scaling factor inferred from Bagpipes, and repeated the fitting 500 times. We added the model template broadening ($\sigma_{\rm template} = 73$ km s^{-1}) in quadrature to recover the intrinsic σ_*. Extended Data Fig. 6 shows the best-fitting SED model for each galaxy compared with the Bagpipes results. The best-fitting parameter values (redshift, σ_* and light-weighted age) are reported in Extended Data Table 4. For J2236+0032, the galaxy SED model that returns from pPXF well agrees with that derived from Bagpipes, confirming the robustness of our measurements. On the other hand, the best-fitting σ_* for J1512+4422 ($\sigma_* = 120$ km s^{-1}) is smaller than that from Bagpipes and is consistent with an unresolved line within its 1σ uncertainty. A part of the reason for this inconsistency is the limited wavelength coverage of the spectrum and the fact that the stellar continuum blueward of Hδ is not well reproduced by both codes. This possibly indicates that there was a large contribution from blueshifted Hδ emission. We, therefore, adopted the 2σ upper limit of <190 km s^{-1} as the σ_* for J1512+4422, which is used in the discussions in the main text and relevant figures, instead of the Bagpipes results.

We also fitted the galaxies without fixing the stellar metallicity. In this case, we found that the metallicity uncertainty for J2236+0032 spanned from subsolar to near-solar values, despite its rich photometric dataset, which indicates that the currently available data are not sufficient to constrain the stellar metallicity.

Number density of post-starburst quasar hosts at $z \approx 6$

Given the redshift range ($6.18 \le z \le 6.40$) and absolute UV magnitude range ($-24.0 \le M_{\rm UV}$ [mag]≤ -21.5) of the SHELLQs sample in the JWST programme, which was drawn from the parent sample of ref. 57, the discovery of two post-starburst galaxies hosting quasars corresponds to a number density of $\log[n\ ({\rm Mpc}^{-3})] = -8.8 \pm 0.3$, where the error reflects the Poisson uncertainty. This number density is approximately 3 dex lower than those of massive quiescent galaxies at similar redshifts ($\log[n\ ({\rm Mpc}^{-3})] = -5.8^{+0.5}_{-0.8}$ at $z = 7.3$)[10], indicating that the quasar phase is short relative to the lifetime of massive galaxies. This difference in number density is even smaller than the ratio of the quasar lifetime to the quenching timescale (1–10 Myr versus a few 100 Myr), as discussed in the main text. A possible explanation is that our selection of quasar-hosting quiescent or quenching galaxies relies on stellar absorption lines, which requires A- and F-type stars to dominate the stellar population and the stellar continuum to remain detectable over the quasar continuum; consequently, our selection is probably incomplete. It is also possible that most quiescent galaxies at high redshift are not quenched by quasar activity.

Double-peak profile in Hα emission from J1512+4422

The NIRSpec data for J1512+4422 exhibit an asymmetric double-peak profile in broad Hα emission with the blue component stronger than the red component (Extended Data Fig. 2). The narrow Hα + [N II] multiplet is observed at the wavelengths expected from its [O III] redshift. It is probable that the double-peak profile of broad Hα originates from nuclear scales, as [O III] is observed as a single line (although it shows some asymmetry in its wings) and there are no signs of a secondary AGN in the NIRCam image (Extended Data Fig. 3b).

Double-peaked broad Balmer lines in AGNs have been shown to arise due to the relativistic Keplerian motion of emitting gas in a geometrically thin and optically thick accretion disk[58]. Following the method described in ref. 59, we used the continuum-subtracted spectrum to fit the Hα + [N II] multiplet with the ref. 60 circular disk model describing the Hα broad emission line region and a double Gaussian model for the narrow emission lines. We found that the double-peaked profile was described well by a circular accretion disk of inclination angle ~26 degrees from face-on with an emitting region extending from 50 to 3,000 gravitational radii, an emissivity versus radius power-law index of 1.5, turbulent broadening of 800 km s^{-1} within the disk, and a single spiral arm of amplitude 7.7 (in contrast to the rest of the disk), a width of 40 degrees and a phase of 300 degrees. The best-fitting disk plus narrow emission line model is shown in Extended Data Fig. 2. The parameters describing the disk are typical of the $z < 0.4$ disk-emitting AGN population[59]. Before this discovery, the highest-redshift double-peak line emitter known was at $z = 1.4$ (ref. 61); J1512+4422 at $z = 6.18$ is the new record-holder. One of the twelve objects in our sample shows a double peak, a fraction consistent with what has been reported at low redshift (3–30%)[58,59,62].

We note that we cannot fully rule out the possibility of the presence of two accreting SMBHs in a single galaxy[63,64] with a separation that is not spatially resolved in our NIRCam images. Candidate binary quasars have been reported with redshifts as high as $z \approx 7$ (refs. 20,65).

Ionized gas outflow

Here we present the profiles of [O III] $\lambda\lambda$4960,5008 emission lines for the two galaxies. Extended Data Fig. 1 shows the continuum-subtracted NIRSpec G395M spectra of the two galaxies, with the best-fitting Gaussian profiles for Hβ emission lines also subtracted. Using QSOFITMORE, we fitted two Gaussian profiles to each doublet line: one representing the narrow 'core' component and the other representing the broad 'wing' component, following the method applied in previous studies[42,66]. We allowed for a velocity shift in the wing component relative to the core component. The line profiles of [O III] λ4960 and [O III] λ5008 were fixed to be the same, other than the scaling factor.

Extended Data Table 1 summarizes the [O III] line profile. We found that both J2236+0032 and J1512+4422 exhibit broad wings in [O III] with full-widths at half-maximum ${\rm FWHM}_{\rm broad} = 2{,}160 \pm 140$ km s^{-1} and $1{,}400 \pm 80$ km s^{-1}, whereas their core components have ${\rm FWHM}_{\rm core} = 330 \pm 40$ km s^{-1} and 350 ± 10 km s^{-1}, respectively. Such broad components have also been seen in other high-redshift quasars[67,68]. Velocity blueshifts are seen for these components with $\Delta v_{\rm wing\text{-}core} = -850 \pm 180$ km s^{-1} and -110 ± 20 km s^{-1}, respectively. J2236+0032 shows the largest velocity offset among the full sample of 12 Subaru HSC quasars observed in our cycle 1 programme. These wing components account for 50–70% of the total [O III] flux. We also found that the [O III] lines of the two targets are spatially extended across the NIRSpec S200A2 slit, even beyond the extraction aperture size (6 pixels). Full analyses of the extended [O III] lines and their interpretation will be presented in C.L.P. et al. (in preparation).

BH mass estimate

This section presents virial black hole mass measurements based on the broad Balmer emission lines and the decomposed quasar continuum. For J2236+0032, we used the prescription of ref. 69 based on Hβ.

This single-epoch mass estimate has an intrinsic scatter of 0.4 dex, which is shown in Figs. 3 and 4. The Hβ linewidth FWHM = 5,650 ± 160 km s^{-1} and the 5,100-Å continuum luminosity $L_{5100} = (1.78 \pm 0.01) \times 10^{45}$ erg s^{-1} were measured from the decomposed quasar spectrum. With a bolometric correction[70] of $L_{bol} = 9.26 L_{5100}$, the inferred bolometric luminosity of J2236+0032 is $L_{bol} = (1.65 \pm 0.01) \times 10^{46}$ erg s^{-1}. From these values, we derived an Hβ-based BH mass $M_{BH} = (1.1 \pm 0.1) \times 10^{9} M_{\odot}$ and an Eddington ratio $L_{bol}/L_{Edd} = 0.12 \pm 0.01$.

The BH mass estimate of J1512+4422 is complicated by its double-peaked Balmer lines, which we modelled as originating from the accretion disk. We here present the BH mass assuming that the single-epoch method can be applied to double-peak emitters, although this assumption is not fully justified, and thus the BH mass of J1512+4422 is uncertain. The FWHM of the broad Hα emission line from the model presented in Extended Data Fig. 2 is 8,590 km s^{-1}. The line luminosity of broad Hα is $L_{H\alpha} = (4.21 \pm 0.03) \times 10^{43}$ erg s^{-1}. We then derived the Hα-based BH mass following ref. 71, which used the Hα FWHM and $L_{H\alpha}$, yielding $M_{BH} = 1.3 \times 10^{9} M_{\odot}$ and an Eddington ratio of 0.03. We use these values in the main text. We also used the prescription of ref. 69, which is based on Hβ FWHM and monochromatic luminosity at rest frame 5,100 Å. The continuum luminosity was measured in the same way as for J2236+0032, giving $L_{5100} = (1.60 \pm 0.01) \times 10^{44}$ erg s^{-1}. Using the Hα linewidth as a proxy for Hβ FWHM results in $M_{BH} = 1.7 \times 10^{9} M_{\odot}$, like what we found above. The Hβ line profile of J1512+4422 is different from that of Hα, for which we measured FWHM = 4,620 km s^{-1}. Directly applying the recipe of ref. 69, we found $M_{BH} = 0.48 \times 10^{9} M_{\odot}$ and $L_{bol}/L_{Edd} = 0.11$. A more detailed analysis and discussions of the BH mass estimate will be presented in our future papers together with our analysis of other HSC quasars observed in JWST cycle 1.

Data availability

The JWST data used in this paper (GO 1967 and GO 3859) can be accessed via the Mikulski Archive for Space Telescopes (https://doi.org/10.17909/mccv-p954).

Code availability

The JWST data were processed with the JWST calibration pipeline (https://jwst-pipeline.readthedocs.io). Public tools were used for data analyses: galight[36] and QSOFitMORE[42].

References

1. Rigby, J. et al. The science performance of JWST as characterized in commissioning. *Publ. Astron. Soc. Pac.* **135**, 048001 (2023).
2. Kennicutt, R. C. & Evans, N. J. Star formation in the Milky Way and nearby galaxies. *Annu. Rev. Astron. Astrophys.* **50**, 531–608 (2012).
3. Carnall, A. C., McLure, R. J., Dunlop, J. S. & Davé, R. Inferring the star formation histories of massive quiescent galaxies with BAGPIPES: evidence for multiple quenching mechanisms. *Mon. Not. R. Astron. Soc.* **480**, 4379–4401 (2018).
4. Carnall, A. C. et al. The VANDELS survey: the star-formation histories of massive quiescent galaxies at 1.0 < *z* < 1.3. *Mon. Not. R. Astron. Soc.* **490**, 417–439 (2019).
5. Kroupa, P. On the variation of the initial mass function. *Mon. Not. R. Astron. Soc.* **322**, 231–246 (2001).
6. Leja, J., Carnall, A. C., Johnson, B. D., Conroy, C. & Speagle, J. S. How to measure galaxy star formation histories. II. Nonparametric models. *Astrophys. J.* **876**, 3 (2019).
7. Pacifici, C. et al. The evolution of star formation histories of quiescent galaxies. *Astrophys. J.* **832**, 79 (2016).
8. Carnall, A. C. et al. A massive quiescent galaxy at redshift 4.658. *Nature* **619**, 716–719 (2023).
9. de Graaff, A. et al. Efficient formation of a massive quiescent galaxy at redshift 4.9. *Nat. Astron.* **9**, 280–292 (2025).
10. Weibel, A. et al. RUBIES reveals a massive quiescent galaxy at *z* = 7.3. *Astrophys. J.* **983**, 11 (2025).
11. Maiolino, R. et al. A small and vigorous black hole in the early Universe. *Nature* **627**, 59–63 (2024).
12. Goulding, A. D. et al. UNCOVER: the growth of the first massive black holes from JWST/NIRSpec-spectroscopic redshift confirmation of an X-ray luminous AGN at *z* = 10.1. *Astrophys. J. Lett.* **955**, L24 (2023).
13. Zhang, H. et al. TRINITY IV: predictions for supermassive black holes at z ≳ 6. *Mon. Not. R. Astron. Soc.* **531**, 4974–4989 (2024).
14. Scoggins, M. T. & Haiman, Z. Diagnosing the massive-seed pathway to high-redshift black holes: statistics of the evolving black hole to host galaxy mass ratio. *Mon. Not. R. Astron. Soc.* **531**, 4584–4597 (2024).
15. Li, W., Inayoshi, K., Onoue, M. & Toyouchi, D. The assembly of black hole mass and luminosity functions of high-redshift quasars via multiple accretion episodes. *Astrophys. J.* **950**, 85 (2023).
16. Davies, F. B., Hennawi, J. F. & Eilers, A.-C. Evidence for low radiative efficiency or highly obscured growth of *z* > 7 quasars. *Astrophys. J. Lett.* **884**, L19 (2019).
17. Eilers, A.-C. et al. EIGER VI. The correlation function, host halo mass and duty cycle of luminous quasars at *z* > 6. *Astrophys. J.* **974**, 275 (2024).
18. Davies, R. I. et al. A close look at star formation around active galactic nuclei. *Astrophys. J.* **671**, 1388–1412 (2007).
19. Wild, V., Heckman, T. & Charlot, S. Timing the starburst-AGN connection. *Mon. Not. R. Astron. Soc.* **405**, 933–947 (2010).
20. Maiolino, R. et al. JADES: the diverse population of infant black holes at 4 < *z* < 11: merging, tiny, poor, but mighty. *Astron. Astrophys.* **691**, A145 (2024).
21. Lupi, A., Quadri, G., Volonteri, M., Colpi, M. & Regan, J. A. Sustained super-Eddington accretion in high-redshift quasars. *Astron. Astrophys.* **686**, A256 (2024).
22. Tanaka, M. et al. Stellar velocity dispersion of a massive quenching galaxy at *z* = 4.01. *Astrophys. J. Lett.* **885**, L34 (2019).
23. Looser, T. J. et al. A recently quenched galaxy 700 million years after the Big Bang. *Nature* **629**, 53–57 (2024).
24. Kormendy, J. & Ho, L. C. Coevolution (or not) of supermassive black holes and host galaxies. *Annu. Rev. Astron. Astrophys.* **51**, 511–653 (2013).
25. Ito, K. et al. COSMOS2020: ubiquitous AGN activity of massive quiescent galaxies at 0 < *z* < 5 revealed by X-ray and radio stacking. *Astrophys. J.* **929**, 53 (2022).
26. Belli, S. et al. Star formation shut down by multiphase gas outflow in a galaxy at a redshift of 2.45. *Nature* **630**, 54–58 (2024).
27. D'Eugenio, F. et al. A fast-rotator post-starburst galaxy quenched by supermassive black-hole feedback at *z* = 3. *Nat. Astron.* **8**, 1443–1456 (2024).
28. Arita, J. et al. Subaru high-*z* exploration of low-luminosity quasars (SHELLQs). XVIII. The dark matter halo mass of quasars at *z* ~ 6. *Astrophys. J.* **954**, 210 (2023).
29. Decarli, R. et al. An ALMA [C II] survey of 27 quasars at *z* > 5.94. *Astrophys. J.* **854**, 97 (2018).
30. Walter, F. et al. ALMA 200 pc imaging of a *z* ~ 7 quasar reveals a compact, disk-like host galaxy. *Astrophys. J.* **927**, 21 (2022).
31. Matsuoka, Y. et al. Subaru high-*z* exploration of low-luminosity quasars (SHELLQs). I. Discovery of 15 quasars and bright galaxies at 5.7 < *z* < 6.9. *Astrophys. J.* **828**, 26 (2016).
32. Matsuoka, Y. et al. Subaru high-*z* exploration of low-luminosity quasars (SHELLQs). X. Discovery of 35 quasars and luminous galaxies at 5.7 ≤ *z* ≤ 7.0. *Astrophys. J.* **883**, 183 (2019).
33. Aihara, H. et al. The Hyper Suprime-Cam SSP Survey: overview and survey design. *Publ. Astron. Soc. Jpn* **70**, S4 (2018).
34. Ding, X. et al. Detection of stellar light from quasar host galaxies at redshifts above 6. *Nature* **621**, 51–55 (2023).
35. Brammer, G. msaexp: NIRSpec analysis tools (0.6.17). *Zenodo* https://doi.org/10.5281/zenodo.8319596 (2023).

36. Ding, X. et al. The mass relations between supermassive black holes and their host galaxies at $1<z<2$ HST-WFC3. *Astrophys. J.* **888**, 37 (2020).
37. Birrer, S. et al. Lenstronomy II: a gravitational lensing software ecosystem. *J. Open Source Softw.* **6**, 3283 (2021).
38. Li, J. et al. Synchronized coevolution between supermassive black holes and galaxies over the last seven billion years as revealed by Hyper Suprime-Cam. *Astrophys. J.* **922**, 142 (2021).
39. Tanaka, T. S. et al. The M_{BH}–M_* relation up to $z\sim2$ through decomposition of COSMOS-Web NIRCam images. *Astrophys. J.* **979**, 215 (2025).
40. Ito, K. et al. Size–stellar mass relation and morphology of quiescent galaxies at $z\geq3$ in public JWST fields. *Astrophys. J.* **964**, 192 (2024).
41. Ding, X. et al. SHELLQs-JWST unveils the host galaxies of twelve quasars at $z>6$. Preprint at https://arxiv.org/abs/2505.03876 (2025).
42. Fu, Y. QSOFITMORE: a Python package for fitting UV-optical spectra of quasars. *Zenodo* https://doi.org/10.5281/zenodo.5810042 (2021).
43. Selsing, J., Fynbo, J. P. U., Christensen, L. & Krogager, J.-K. An X-Shooter composite of bright $1<z<2$ quasars from UV to infrared. *Astron. Astrophys.* **585**, A87 (2016).
44. Goto, T. et al. Hδ-strong galaxies in the Sloan Digital Sky Survey. I. The catalog. *Publ. Astron. Soc. Jpn* **55**, 771–787 (2003).
45. Wu, P.-F. Ejective feedback as a quenching mechanism in the first 1.5 billion years of the Universe: detection of neutral gas outflow in a $z=4$ recently quenched galaxy. *Astrophys. J.* **978**, 131 (2025).
46. Curtis-Lake, E. et al. Spectroscopic confirmation of four metal-poor galaxies at $z=10.3$–13.2. *Nat. Astron.* **7**, 622–632 (2023).
47. Inayoshi, K. & Maiolino, R. Extremely dense gas around little red dots and high-redshift AGNs: a non-stellar origin of the Balmer break and absorption features. *Astrophys. J. Lett.* **980**, L27 (2025).
48. Bruzual, G. & Charlot, S. Stellar population synthesis at the resolution of 2003. *Mon. Not. R. Astron. Soc.* **344**, 1000–1028 (2003).
49. Chevallard, J. & Charlot, S. Modelling and interpreting spectral energy distributions of galaxies with BEAGLE. *Mon. Not. R. Astron. Soc.* **462**, 1415–1443 (2016).
50. Falcón-Barroso, J. et al. An updated MILES stellar library and stellar population models. *Astron. Astrophys.* **532**, A95 (2011).
51. Calzetti, D. et al. The dust content and opacity of actively star-forming galaxies. *Astrophys. J.* **533**, 682–695 (2000).
52. Nakajima, K. et al. JWST census for the mass-metallicity star formation relations at $z=4$–10 with self-consistent flux calibration and proper metallicity calibrators. *Astrophys. J. Suppl. Ser.* **269**, 33 (2023).
53. Greene, J. E. & Ho, L. C. Measuring stellar velocity dispersions in active galaxies. *Astrophys. J.* **641**, 117–132 (2006).
54. Cappellari, M. Full spectrum fitting with photometry in PPXF: stellar population versus dynamical masses, non-parametric star formation history and metallicity for 3200 LEGA-C galaxies at redshift $z\approx0.8$. *Mon. Not. R. Astron. Soc.* **526**, 3273–3300 (2023).
55. Conroy, C., Gunn, J. E. & White, M. The propagation of uncertainties in stellar population synthesis modeling. I. The relevance of uncertain aspects of stellar evolution and the initial mass function to the derived physical properties of galaxies. *Astrophys. J.* **699**, 486–506 (2009).
56. Conroy, C. & Gunn, J. E. The propagation of uncertainties in stellar population synthesis modeling. III. Model calibration, comparison, and evaluation. *Astrophys. J.* **712**, 833–857 (2010).
57. Matsuoka, Y. et al. Subaru high-*z* exploration of low-luminosity quasars (SHELLQs). V. Quasar luminosity function and contribution to cosmic reionization at $z=6$. *Astrophys. J.* **869**, 150 (2018).
58. Eracleous, M., Lewis, K. T. & Flohic, H. M. L. G. Double-peaked emission lines as a probe of the broad-line regions of active galactic nuclei. *New Astron. Rev.* **53**, 133–139 (2009).
59. Ward, C. et al. Panic at the ISCO: time-varying double-peaked broad lines from evolving accretion disks are common among optically variable AGNs. *Astrophys. J.* **961**, 172 (2024).
60. Chen, K. & Halpern, J. P. Structure of line-emitting accretion disks in active galactic nuclei: ARP 102B. *Astrophys. J.* **344**, 115 (1989).
61. Luo, B. et al. Discovery of the most distant double-peaked emitter at $z=1.369$. *Astrophys. J.* **695**, 1227–1232 (2009).
62. Strateva, I. V. et al. Double-peaked low-ionization emission lines in active galactic nuclei. *Astron. J.* **126**, 1720–1749 (2003).
63. Xu, D. & Komossa, S. Narrow double-peaked emission lines of SDSS J131642.90+175332.5: signature of a single or a binary AGN in a merger, jet-cloud interaction, or unusual narrow-line region geometry. *Astrophys. J. Lett.* **705**, L20–L24 (2009).
64. Smith, K. L. et al. A search for binary active galactic nuclei: double-peaked [O III] AGNs in the Sloan Digital Sky Survey. *Astrophys. J.* **716**, 866–877 (2010).
65. Übler, H. et al. GA-NIFS: JWST discovers an offset AGN 740 million years after the big bang. *Mon. Not. R. Astron. Soc.* **531**, 355–365 (2024).
66. Bischetti, M. et al. The WISSH quasars project. I. Powerful ionised outflows in hyper-luminous quasars. *Astron. Astrophys.* **598**, A122 (2017).
67. Marshall, M. A. et al. GA-NIFS: black hole and host galaxy properties of two $z\simeq6.8$ quasars from the NIRSpec IFU. *Astron. Astrophys.* **678**, A191 (2023).
68. Yang, J. et al. A spectroscopic survey of biased halos in the reionization era (ASPIRE): a first look at the rest-frame optical spectra of $z>6.5$ quasars using JWST. *Astrophys. J. Lett.* **951**, L5 (2023).
69. Vestergaard, M. & Peterson, B. M. Determining central black hole masses in distant active galaxies and quasars. II. Improved optical and UV scaling relationships. *Astrophys. J.* **641**, 689–709 (2006).
70. Richards, G. T. et al. Spectral energy distributions and multiwavelength selection of type 1 quasars. *Astrophys. J. Suppl. Ser.* **166**, 470–497 (2006).
71. Greene, J. E. & Ho, L. C. Estimating black hole masses in active galaxies using the Hα emission line. *Astrophys. J.* **630**, 122–129 (2005).
72. Salmon, B. et al. The relation between star formation rate and stellar mass for galaxies at $3.5\leq z\leq6.5$ in CANDELS. *Astrophys. J.* **799**, 183 (2015).
73. Izumi, T. et al. Subaru high-*z* exploration of low-luminosity quasars (SHELLQs). XIII. Large-scale feedback and star formation in a low-luminosity quasar at $z=7.07$ on the local black hole to host mass relation. *Astrophys. J.* **914**, 36 (2021).
74. Schreiber, C. et al. Near infrared spectroscopy and star-formation histories of $3\leq z\leq4$ quiescent galaxies. *Astron. Astrophys.* **618**, A85 (2018).
75. Valentino, F. et al. Quiescent galaxies 1.5 billion years after the Big Bang and their progenitors. *Astrophys. J.* **889**, 93 (2020).
76. Forrest, B. et al. The massive ancient galaxies at $z>3$ near-infrared (MAGAZ3NE) survey: confirmation of extremely rapid star formation and quenching timescales for massive galaxies in the early Universe. *Astrophys. J.* **903**, 47 (2020).
77. Carnall, A. C. et al. The JWST EXCELS survey: too much, too young, too fast? Ultra-massive quiescent galaxies at $3<z<5$. *Mon. Not. R. Astron. Soc.* **534**, 325–348 (2024).
78. Nanayakkara, T. et al. A population of faint, old, and massive quiescent galaxies at $3<z<4$ revealed by JWST NIRSpec Spectroscopy. *Sci. Rep.* **14**, 3724 (2024).
79. Kakimoto, T. et al. A massive quiescent galaxy in a group environment at $z=4.53$. *Astrophys. J.* **963**, 49 (2024).

80. Glazebrook, K. et al. A massive galaxy that formed its stars at $z \approx 11$. *Nature* **628**, 277–281 (2024).
81. Wang, B. et al. RUBIES: evolved stellar populations with extended formation histories at $z \sim 7$–8 in candidate massive galaxies identified with JWST/NIRSpec. *Astrophys. J. Lett.* **969**, L13 (2024).
82. Kokorev, V. et al. Silencing the giant: evidence of active galactic nucleus feedback and quenching in a little red dot at $z = 4.13$. *Astrophys. J.* **975**, 178 (2024).
83. Labbe, I. et al. An unambiguous AGN and a Balmer break in an ultraluminous little red dot at $z = 4.47$ from ultradeep UNCOVER and all the little things spectroscopy. Preprint at https://arxiv.org/abs/2412.04557 (2024).
84. Stone, M. A., Lyu, J., Rieke, G. H. & Alberts, S. Detection of the low-stellar-mass host galaxy of a $z = 6.25$ quasar with JWST. *Astrophys. J.* **953**, 180 (2023).
85. Stone, M. A., Lyu, J., Rieke, G. H., Alberts, S. & Hainline, K. N. Undermassive host galaxies of five $z \sim 6$ luminous quasars detected with JWST. *Astrophys. J.* **964**, 90 (2024).
86. Yue, M. et al. EIGER. V. Characterizing the host galaxies of luminous quasars at $z \gtrsim 6$. *Astrophys. J.* **966**, 176 (2024).
87. Matsuoka, Y. et al. The Sloan Digital Sky Survey reverberation mapping project: post-starburst signatures in quasar host galaxies at $z > 1$. *Astrophys. J.* **811**, 91 (2015).

Acknowledgements

We thank A. C. Carnall for supporting our use of Bagpipes. We thank Y. Fu for his help on the use of QSOFitMORE. We thank J. Greene, S. Toft, T. Kakimoto and M. Tanaka for fruitful discussions. This work is based on observations made with the NASA/ESA/CSA JWST. The data were obtained from the Mikulski Archive for Space Telescopes at the Space Telescope Science Institute, which is operated by the Association of Universities for Research in Astronomy, under NASA contract NAS 5-03127 for JWST. These observations are associated with programmes GO 1967 and GO 3859. Support for these programmes was provided by NASA through a grant from the Space Telescope Science Institute. This work was supported by World Premier International Research Center Initiative, MEXT, Japan. This work used computing resources at Kavli IPMU. M.O., X.D., J.D.S., Y.M., T.I., K. Ito, K.K. and H.U. are supported by the Japan Society for the Promotion of Science (KAKENHI Grant Numbers JP24K22894, JP22K14071, JP18H01251, JP22H01262, JP21H04494, JP20K14531, JP23K13141, JP17H06130 and JP20H01953). M.O. and K. Inayoshi acknowledge support from the National Natural Science Foundation of China (Grant Numbers 12150410307, 12073003, 11721303, 11991052 and 11950410493). K. Inayoshi acknowledges support from the China Manned Space Project (Grant Numbers CMS-CSST-2021-A04 and CMS-CSST-2021-A06). S.E.I.B. is funded by the Deutsche Forschungsgemeinschaft (German Research Foundation) under Emmy Noether Grant Number BO 5771/1-1. Z.H., T.T. and M.S. acknowledge support from the NSF (Grant Numbers AST-2006176, AST-1907208 and AST-2006177). A.L. acknowledges funding from MUR (Grant Number PRIN 2022935STW). B.T. acknowledges support from the European Research Council (ERC) under the European Union's Horizon 2020 research and innovation programme (Grant Agreement Number 950533) and from the Israel Science Foundation (Grant Number 1849/19). F. Walter acknowledges support from the ERC (Grant Cosmic_gas). J.-T.S. is supported by the Deutsche Forschungsgemeinschaft (Project Number 518006966). M.T. acknowledges support from the NWO (Grant Number 0.16.VIDI.189.162, ODIN). S.F. acknowledges support from NASA through the NASA Hubble Fellowship (Grant Number HST-HF2-51505.001-A awarded by the Space Telescope Science Institute). K. Iwasawa acknowledges support under Grant Number PID2022-136827NB-C44 funded by MCIN/AEI/10.13039/501100011033 /FEDER, EU. M. Vestergaard gratefully acknowledges financial support from the Independent Research Fund Denmark (Grant Numbers DFF 8021-00130 and 3103-00146). F. Wang acknowledges support from the NSF (Award Number AST-2513040). R.B. is supported by the SNSF through the Ambizione Grant PZ00P2_223532.

Author contributions

M.O. led the preparation of the observation programme, data reduction, spectroscopic data analysis and preparing the paper. X.D. led the imaging data analysis and contributed to the relevant sections of the paper. We regard these first two authors (M.O. and X.D.) as having contributed equally to this work. J.D.S. and M.A.S. provided consulting on paper preparation. Y.M. contributed to the discovery of the two quasars analysed in this paper. C.W. led the spectral analysis of the double-peak line shape of the Hα emission in the spectrum of J1512+4422. C.L.P. performed the NIRSpec 2D spectroscopic analysis and evaluated the strength of the extended Hα emission. M.T.S. and H.Z. provided theoretical model predictions on the SMBH and host stellar growth history of J2236+0032 presented in Fig. 3. K. Ito contributed to the SED analysis of the two galaxies based on pPXF. M.O., X.D., J.D.S., Y.M., T.I., M.A.S., C.L.P. and K.J. led the project design and management and also developed the main interpretation of the results. I.T.A., K.A., J.A., S.B., R.B., S.E.I.B., A.-C.E., S.F., M.H., Z.H., M.I., K. Inayoshi, K. Iwasawa, N.K., T.K., K.K., C.-H.L., J. Li, A.L., J. Lyu, T.N., R.O., J.-T.S., M.S., K.S., Y.T., B.T., M.T., T.T., H.U., B.V., M. Volonteri, M. Vestergaard, F. Walter, F. Wang and J.Y contributed to the discussion of the results presented and to paper preparation.

Competing interests

The authors declare no competing interests.

Additional information

Extended data is available for this paper at https://doi.org/10.1038/s41550-025-02628-1.

Correspondence and requests for materials should be addressed to Masafusa Onoue or Xuheng Ding.

Peer review information *Nature Astronomy* thanks Francesco D'Eugenio, Minghao Yue and the other, anonymous, reviewer(s) for their contribution to the peer review of this work.

Reprints and permissions information is available at www.nature.com/reprints.

Masafusa Onoue[1,2,3,4,5]✉, **Xuheng Ding**[1,6]✉, **John D. Silverman**[1,3,7,8], **Yoshiki Matsuoka**[9], **Takuma Izumi**[7,10,11,12], **Michael A. Strauss**[13], **Charlotte Ward**[13], **Camryn L. Phillips**[13], **Kei Ito**[7,14,15], **Irham T. Andika**[16,17], **Kentaro Aoki**[18], **Junya Arita**[7], **Shunsuke Baba**[19], **Rebekka Bieri**[20], **Sarah E. I. Bosman**[4,21], **Anna-Christina Eilers**[22], **Seiji Fujimoto**[23], **Melanie Habouzit**[4,24], **Zoltan Haiman**[25,26,27], **Masatoshi Imanishi**[10,11], **Kohei Inayoshi**[2], **Kazushi Iwasawa**[28,29], **Knud Jahnke**[4], **Nobunari Kashikawa**[7,30], **Toshihiro Kawaguchi**[31], **Kotaro Kohno**[30,32], **Chien-Hsiu Lee**[33], **Junyao Li**[34], **Alessandro Lupi**[35], **Jianwei Lyu**[36], **Tohru Nagao**[9], **Roderik Overzier**[37], **Jan-Torge Schindler**[38], **Malte Schramm**[39], **Matthew T. Scoggins**[25], **Kazuhiro Shimasaku**[7,30], **Yoshiki Toba**[10,40,41], **Benny Trakhtenbrot**[42], **Maxime Trebitsch**[43], **Tommaso Treu**[44], **Hideki Umehata**[45,46], **Bram Venemans**[37], **Marianne Vestergaard**[36,47], **Marta Volonteri**[48], **Fabian Walter**[4], **Feige Wang**[49], **Jinyi Yang**[49] & **Haowen Zhang**[36]

---

[1]Kavli Institute for the Physics and Mathematics of the Universe (WPI), The University of Tokyo Institutes for Advanced Study, The University of Tokyo, Kashiwa, Japan. [2]Kavli Institute for Astronomy and Astrophysics, Peking University, Beijing, China. [3]Center for Data-Driven Discovery, Kavli IPMU (WPI), UTIAS, The University of Tokyo, Kashiwa, Japan. [4]Max-Planck-Institut für Astronomie, Heidelberg, Germany. [5]Waseda Institute for Advanced Study (WIAS), Waseda University, Tokyo, Japan. [6]School of Physics and Technology, Wuhan University, Wuhan, China. [7]Department of Astronomy, School of Science, The University of Tokyo, Tokyo, Japan. [8]Center for Astrophysical Sciences, Department of Physics and Astronomy, Johns Hopkins University, Baltimore, MD, USA. [9]Research Center for Space and Cosmic Evolution, Ehime University, Matsuyama, Japan. [10]National Astronomical Observatory of Japan, Tokyo, Japan. [11]Graduate Institute for Advanced Studies, SOKENDAI, Tokyo, Japan. [12]Kagoshima University, Kagoshima, Japan. [13]Department of Astrophysical Sciences, Princeton University, Princeton, NJ, USA. [14]Cosmic Dawn Center (DAWN), Copenhagen, Denmark. [15]DTU Space, Technical University of Denmark, Kongens Lyngby, Denmark. [16]Department of Physics, TUM School of Natural Sciences, Technical University of Munich, Garching, Germany. [17]Max-Planck-Institut für Astrophysik, Garching, Germany. [18]Subaru Telescope, National Astronomical Observatory of Japan, Hilo, HI, USA. [19]Institute of Space and Astronautical Science, Japan Aerospace Exploration Agency, Sagamihara, Japan. [20]Department of Astrophysics, University of Zurich, Zurich, Switzerland. [21]Institute for Theoretical Physics, Heidelberg University, Heidelberg, Germany. [22]MIT Kavli Institute for Astrophysics and Space Research, Cambridge, MA, USA. [23]Department of Astronomy, The University of Texas at Austin, Austin, TX, USA. [24]Department of Astronomy, University of Geneva, Chemin d'Ecogia, CH-1290 Versoix, Switzerland. [25]Department of Astronomy, Columbia University, New York, NY, USA. [26]Department of Physics, Columbia University, New York, NY, USA. [27]Institute of Science and Technology Austria (ISTA), Klosterneuburg, Austria. [28]Institut de Ciències del Cosmos (ICCUB), Universitat de Barcelona (IEEC-UB), Barcelona, Spain. [29]ICREA, Barcelona, Spain. [30]Research Center for the Early Universe, The University of Tokyo, Tokyo, Japan. [31]Graduate School of Science and Engineering, University of Toyama, Toyama, Japan. [32]Institute of Astronomy, Graduate School of Science, The University of Tokyo, Tokyo, Japan. [33]W. M. Keck Observatory, Kamuela, HI, USA. [34]Department of Astronomy, University of Illinois at Urbana-Champaign, Urbana, IL, USA. [35]Dipartimento di Scienza e Alta Tecnologia, Università degli Studi dell'Insubria, Como, Italy. [36]Steward Observatory, University of Arizona, Tucson, AZ, USA. [37]Leiden Observatory, Leiden University, Leiden, the Netherlands. [38]Hamburger Sternwarte, University of Hamburg, Hamburg, Germany. [39]Universität Potsdam, Potsdam, Germany. [40]Department of Physical Sciences, Ritsumeikan University, Kusatsu, Japan. [41]Academia Sinica Institute of Astronomy and Astrophysics, Taipei, Taiwan. [42]School of Physics and Astronomy, Tel Aviv University, Tel Aviv, Israel. [43]Kapteyn Astronomical Institute, University of Groningen, Groningen, the Netherlands. [44]Department of Physics and Astronomy, University of California, Los Angeles, CA, USA. [45]Institute for Advanced Research, Nagoya University, Nagoya, Japan. [46]Department of Physics, Graduate School of Science, Nagoya University, Nagoya, Japan. [47]DARK, Niels Bohr Institute, Copenhagen, Denmark. [48]Institut d'Astrophysique de Paris, CNRS, Sorbonne Université, Paris, France. [49]Department of Astronomy, University of Michigan, Ann Arbor, MI, USA. ✉e-mail: masafusa.onoue@aoni.waseda.jp; dingxh@whu.edu.cn

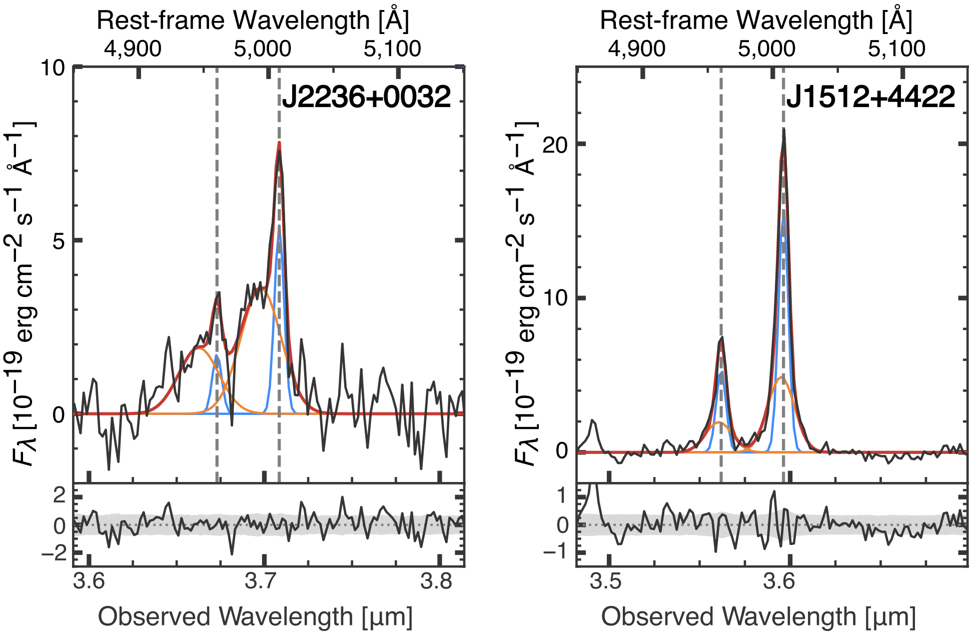

Extended Data Fig. 1 | [O III] ionized gas profile. Left and right panels show the spectrum of J2230 + 0032 and J1512 + 4422, respectively (black). The best-fit models for the continuum, iron, and Hβ line emissions are subtracted for illustration purposes. The core and broad wing components modeled as Gaussian profiles are shown with blue and orange lines, respectively. The total profiles of the best-fit emission line models are shown with red lines. The rest-frame wavelengths indicated at the top, as well as the expected locations of each doublet line (grey dashed lines) are based on redshifts estimated from the Balmer absorption lines. In the bottom panels, the residuals are shown in black lines, and the ± 1σ flux uncertainty at each pixel is indicated as grey shades.

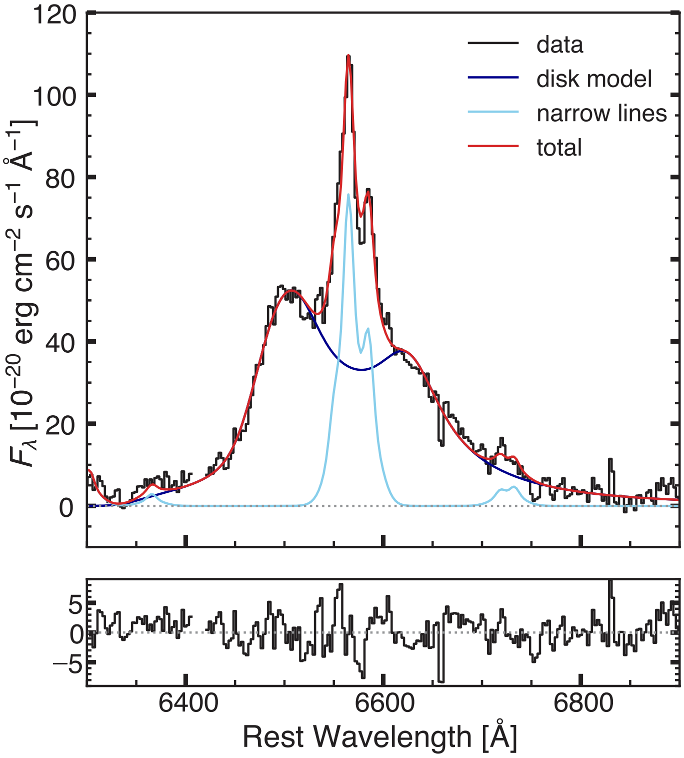

Extended Data Fig. 2 | Double-peaked H*α* emission for J1512 + 4422. The observed H*α* profile (after continuum subtraction) is shown in black. Our model fit based on the method presented in ref. 59 is shown as colored lines (dark blue: disk model, light blue: narrow lines, red: total). The wavelength and the flux density are presented in the rest frame. The bottom panel shows the residual fluxes, that is, the difference between the observed profile and the best-fit model.

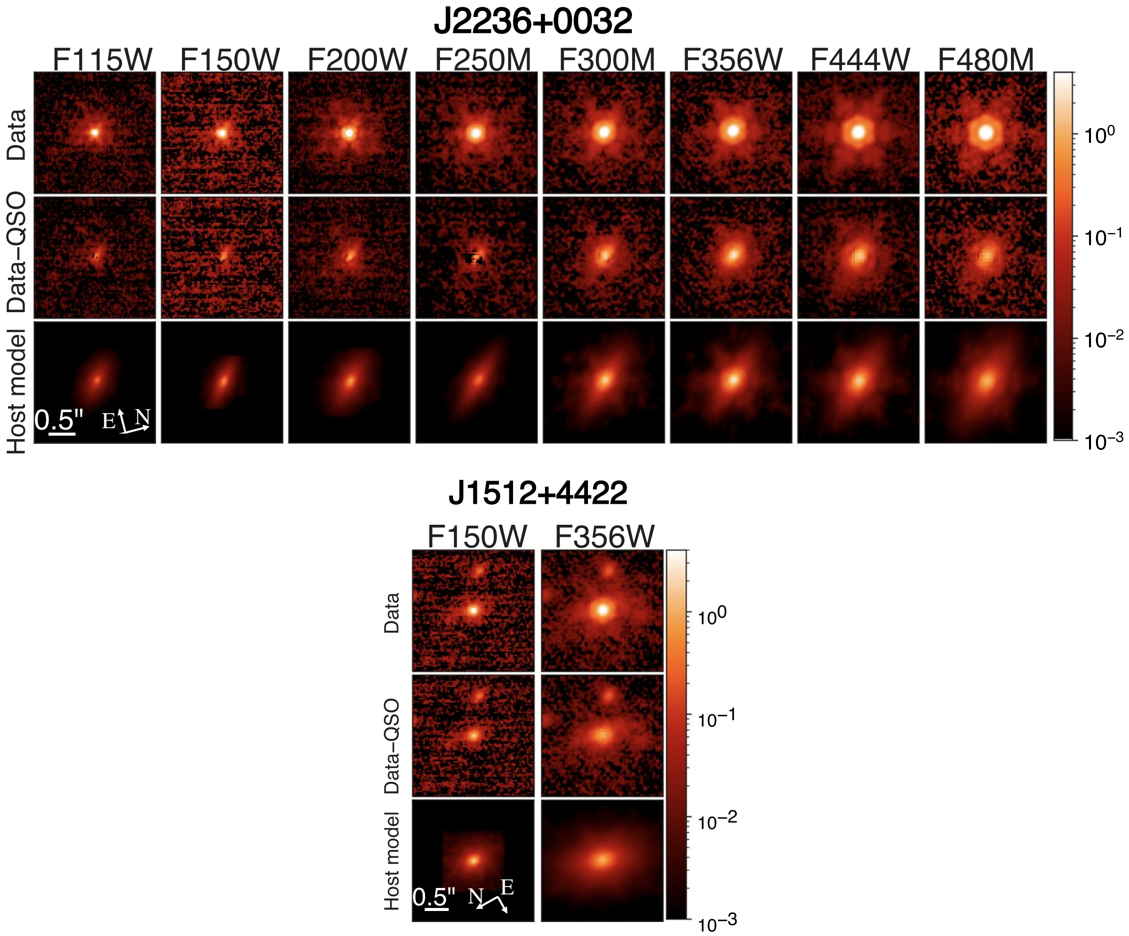

Extended Data Fig. 3 | Host galaxy detection of J2236 + 0032 (top) and J1512 + 4422 (bottom). For each quasar, we present the original NIRCam image, the PSF-subtracted host galaxy-only image, and the best-fit host galaxy model in a vertical order. Data are presented from F115W filter to F480M for J2236+0032, and F150W and F356W for J1512+4422. The image scale of each panel is 2″ × 2″, with flux density shown on a logarithmic scale in units of megajansky per steradian. Arrows in the lower left panels indicate the North and East directions.

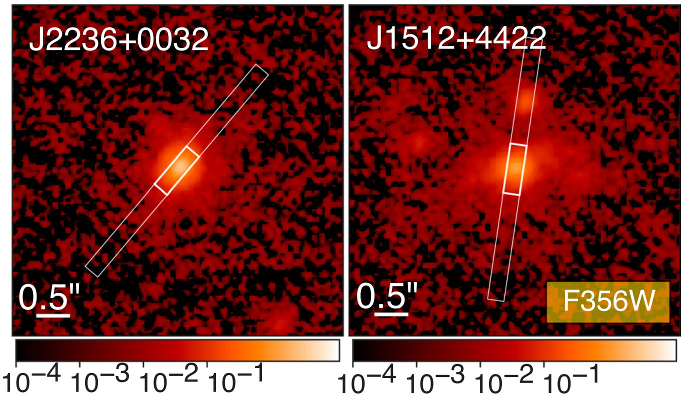

Extended Data Fig. 4 | NIRSpec Fixed-Slit alignment onto the host galaxies. For each galaxy, the outer rectangle indicates the S200A2 slit position and the inner rectangle indicates the extraction aperture of the 1D spectrum. The background images are the decomposed host images in F356W.

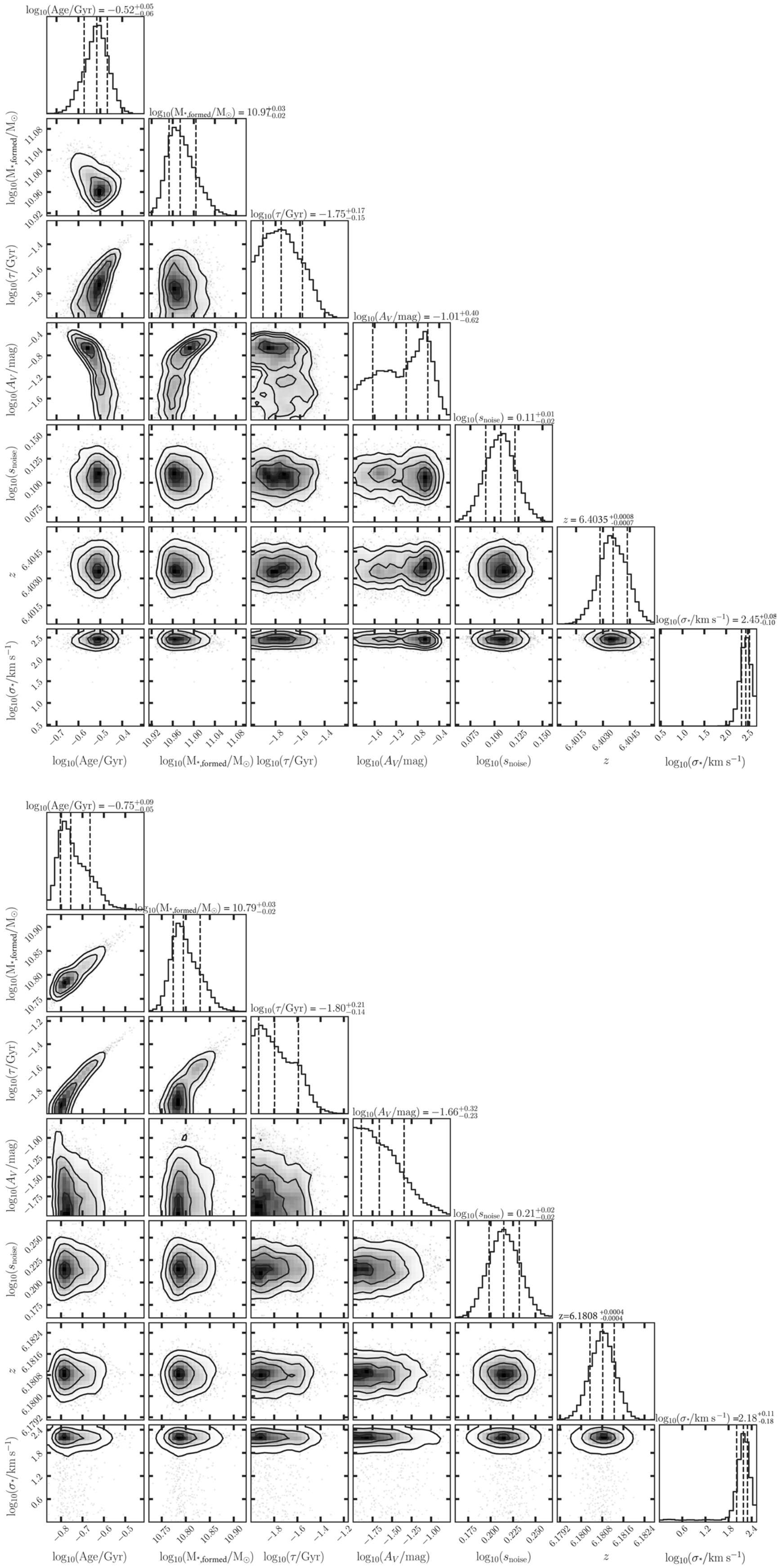

Extended Data Fig. 5 | Example posterior distribution of the Bagpipes SED fitting. The top and bottom panels show J2236 + 0032, and J1512 + 4422, respectively. The delayed-τ SFH model is presented for each galaxy. Note that the stellar mass fitted in Bagpipes ($\log M_{*,\mathrm{formed}}$) represents the total formed stellar mass, from which the observed stellar mass ($\log M_*$) is derived.

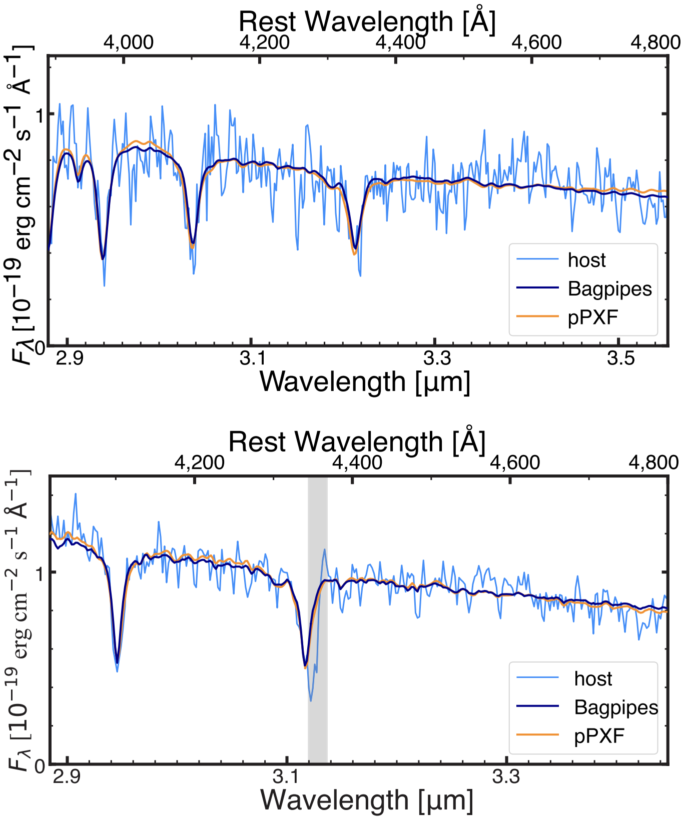

Extended Data Fig. 6 | Comparison of spectral fitting results using two different methods. The top and bottom panels show the decomposed host spectrum (light blue) for J2236 + 0032 and J1512 + 4422, respectively. The best-fit models from Bagpipes (dark blue) and pPXF (orange) are overlaid. The red wing of the Hγ absorption of J1512 + 4422, shown as gray shade, is masked in the spectral fitting.

Extended Data Table 1 | [O III] line profile

ID	$z_{\mathrm{[OIII]}}$	$\Delta v_{\mathrm{wing-core}}$ [km s^{-1}]	FWHM$_{\mathrm{core}}$ [km s^{-1}]	FWHM$_{\mathrm{wing}}$ [km s^{-1}]
J2236+0032	6.4047 ± 0.0006	-850 ± 50	330 ± 40	2160 ± 140
J1512+4422	6.1806 ± 0.0004	-110 ± 20	350 ± 10	1400 ± 80

The [O III] redshifts are based on the core components. $\Delta v_{\mathrm{wing-core}}$ is the velocity offset of the wing component of [O III]. The negative values correspond to velocity blueshifts. Instrumental broadening is corrected for the line widths.

Extended Data Table 2 | NIRCam photometry of the two quasars and their host galaxies

ID	J2236+0032		J1512+4422	
	QSO	Host	QSO	Host
F115W	23.12 ± 0.03	25.36 ± 0.16	⋯	⋯
F150W	22.74 ± 0.01	24.93 ± 0.10	23.69 ± 0.05	23.95 ± 0.05
F200W	22.26 ± 0.01	24.44 ± 0.09	⋯	⋯
F250M	22.12 ± 0.07	24.14 ± 0.44	⋯	⋯
F300M	22.08 ± 0.06	23.04 ± 0.11	⋯	⋯
F356W	22.04 ± 0.10	22.87 ± 0.20	22.51 ± 0.05	22.95 ± 0.06
F444W	21.93 ± 0.04	22.68 ± 0.08	⋯	⋯
F480M	21.42 ± 0.01	22.85 ± 0.05	⋯	⋯

The Sérsic index is fixed to $n = 3$ for the host galaxy model in each case.

Extended Data Table 3 | Host effective radius R_{eff} and minor-to-major axis ratio $q(=b/a)$ in F356W

ID	R_{eff} [$''$]	R_{eff} [kpc]	q
J2236+0032	0.10±0.01	0.55±0.06	0.34±0.04
J1512+4422	0.17±0.02	0.96±0.11	0.53±0.02

We report the host sizes in both arcseconds and physical scale (proper kiloparsecs).

Extended Data Table 4 | Quasar and Host SED parameters obtained from Bagpipes and pPXF

ID	J2236+0032		J1512+4422	
SFH	delayed τ	non-parametric	delayed τ	non-parametric
(Bagpipes)				
z	$6.4035^{+0.0008}_{-0.0007}$	$6.4036^{+0.0007}_{-0.0007}$	$6.1808^{+0.0004}_{-0.0004}$	$6.1808^{+0.0004}_{-0.0003}$
$\log M_*/M_\odot$	$10.80^{+0.03}_{-0.02}(\pm 0.08)$	$10.85^{+0.02}_{-0.02}(\pm 0.08)$	$10.64^{+0.04}_{-0.01}(\pm 0.02)$	$10.68^{+0.04}_{-0.02}(\pm 0.02)$
mass-weighted age [Myr]	270^{+20}_{-30}	400^{+30}_{-50}	150^{+20}_{-20}	190^{+50}_{-30}
τ [Myr]	18^{+9}_{-5}	$\cdots$	16^{+10}_{-5}	$\cdots$
A_V [mag]	$0.09^{+0.15}_{-0.07}$	$0.05^{+0.08}_{-0.03}$	$0.02^{+0.02}_{-0.01}$	$0.02^{+0.02}_{-0.01}$
σ_* [km s^{-1}]	290^{+50}_{-60}	280^{+50}_{-50}	160^{+30}_{-40}	150^{+40}_{-50}
noise scaling factor	$1.28^{+0.04}_{-0.04}$	$1.28^{+0.04}_{-0.04}$	$1.65^{+0.06}_{-0.07}$	$1.65^{+0.06}_{-0.05}$
(pPXF)				
z	6.3999 ± 0.0017		6.1797 ± 0.0009	
σ_* [km s^{-1}]	270 ± 60		< 190 (2σ)	
light-weighted age [Myr]	320^{+50}_{-10}		250^{+80}_{-20}	

There are two error budgets reported for the stellar mass: one from the SED fitting inference and the other (in parentheses) originating from the decomposed host galaxy photometry in F356W. Stellar mass uncertainties due to the choice of the IMF are not take into account. A 2σ upper limit on σ_* is reported for J1512 + 4422 from the pPXF measurement (see Methods).